8-2013

Structural characterization of the Redox-Dependent differences in the Cytochrome P450cam-Putidaredoxin Complex using solution NMR spectroscopy

Nicholas John Lopes
nlopes@utk.edu

To the Graduate Council:

I am submitting herewith a thesis written by Nicholas John Lopes entitled "Structural characterization of the Redox-Dependent differences in the Cytochrome P450cam-Putidaredoxin Complex using solution NMR spectroscopy." I have examined the final electronic copy of this thesis for form and content and recommend that it be accepted in partial fulfillment of the requirements for the degree of Master of Science, with a major in Biochemistry and Cellular and Molecular Biology.

Nitin U. Jain, Major Professor

We have read this thesis and recommend its acceptance:

Jerome Baudry, Engin Serpersu

Accepted for the Council:
Dixie L. Thompson

Vice Provost and Dean of the Graduate School

(Original signatures are on file with official student records.)

Structural characterization of the Redox-Dependent differences in the Cytochrome P450cam-Putidaredoxin Complex using solution NMR spectroscopy

A Thesis Presented for the
Master of Science
Degree
The University of Tennessee, Knoxville

Nicholas John Lopes

August 2013

DEDICATION

To my father Anthony, for the kick in the ass.

ACKNOWLEDGEMENTS

For his intrepid belief in me, I acknowledge my advisor Dr. Nitin Jain. For use of their anaerobic facilities, I acknowledge the Center for Environmental Biotechnology. For his instruction with NMR processing, I acknowledge Carey Cantrell.

ABSTRACT

Complexation between proteins as part of biological electron transfer reactions is driven by precise interactions that are often characterized by short lifetimes, weak affinities and high turnover rates. These complex interactions are difficult to study structurally in physiologically relevant oxidation states due to their transient nature and/or large molecular sizes. One such protein complex in the cytochrome P450 family of enzymes that is of great interest to researchers due to its prototypical nature is the Putidaredoxin (Pdx)- cytochrome P450cam (CYP101) electron transfer complex that is involved in hydroxylation of D-camphor in the bacterium *Pseudomonas putida*. While the individual protein structures for Pdx and CYP101 have been known for several years in both oxidized and reduced states, high-resolution structural information for the Pdx-CYP101 complex is still lacking in either oxidation state. This structural information is critical to not only determine the electron transfer pathway between the two proteins in this complex, but also to explain the role of Pdx as an effector in substrate turnover.

In this study, a solution NMR approach utilizing long-range distance restraints derived from paramagnetic relaxation effects is used to obtain structures of the Pdx-CYP101 complex in both substrate-bound oxidized and a catalytically competent reduced form. Key redox-dependent structural and dynamic differences between the two complexes have been characterized which provide insights into the mechanism of effector activity of Pdx.

TABLE OF CONTENTS

LIST OF TABLES

LIST OF FIGURES

CHAPTER I
INTRODUCTION AND BACKGROUND

1.1 Electron Transfer in Biological Systems

Biological electron transfer (BET) is a vital process for all life. Signal transduction, energy transformation, and cell growth all depend on the spatial and temporal control of BET for maintaining homeostasis (1). Frequently, BET manifests as a specific sequence of tightly regulated protein shuttles that rely on precise redox partner recognition in order to prevent “short circuits” (2). Requisite short lifetimes, weak affinities, and high turnover rates often characterize the protein-protein interactions in BET systems. Complexation between proteins is therefore optimized to achieve transient lifetimes on the order of milliseconds (3). Communication through multiple specific binding sites commonly allow electron transport proteins to relay between two components of a cascade (4). Structural features such as low geometric complementarity and poor packing density tend to define these interactions, and allow for the necessary balance between promiscuity and discrimination. Unfortunately, the features that enable efficient protein electron transfer such as fast dissociation rates and complicated molecular surfaces, also make them difficult to study, particularly from a structural perspective.

1.2 Cytochrome P450s

A prominent example of an enzyme system reliant on efficient BET for functionality is that of cytochrome P450. As a ubiquitous super family of heme-containing monoxygenases, P450s stereo- and regio-specifically target a diverse range of organic, hydrophobic substrates for the incorporation of one atom of molecular oxygen into a relatively inert carbon site according to the general reaction scheme in Eq. (1):

$$RH + O_2 + 2e- + 2\ H^+ \rightarrow R\text{-}OH + H_2O \quad (1)$$

The two electrons required for the monoxygenation are initially donated from NAD(P)H, and depend on a series of protein-protein interactions for efficient delivery to the P450 catalyst (5). With some exceptions, two classes of electron relay systems have been defined for cytochrome P450s that are largely divided along their prokaryotic or eukaryotic origins. Class I prokaryotic systems involve three soluble and cytosolic proteins in a cascade that begins with a NADH-dependent FAD-binding reductase (FdR). FdR transfers an electron to a [2Fe-2S] ferredoxin (Fdx) which ultimately reduces the P450. Alternatively, the class II eukaryotic system most commonly involves only two membrane bound constituents; the P450 and a diflavin NADPH-Cytochrome P450 reductase (CPR). Depending on its subcellular localization, eukaryotic P450s can be accompanied by another reducing partner cytochrome *b5* which synergistically cooperates with CPR to improve catalytic efficiency (6-8).

By hydroxylating substrates, P450s increase their polarity and effectively solubilize them for downstream conjugation or excretion. While the most common chemistry performed by P450s is the hydroxylation of aliphatic and aromatic hydrocarbons; they are capable of myriad reactions, including but not limited to: alkene and arene epoxidation, oxidative deamination, dehalogenation, and decarboxylation (9). These reactions enable a variety of physiological processes such as; xenobiotic degradation, steroidogenesis, fatty acid metabolism, and the activation of procarcinogens.

Their leading role in the phase I bio-transformation of ~90% of pharmaceuticals makes them the focus of two major concerns in clinical pharmacology, drug-drug interactions and polymorphism pharmacokinetics (7). With such a remarkable breadth of substrates and a profound commercial relevance, much work in P450 research has gone into explaining the catalytic mechanism and basis for ligand recognition. A better understanding of inter-individual variations and the structural basis for ligand promiscuity will ultimately aid in the early computational phases of drug discovery, and facilitate prediction of drug interactions (10). Pharmaceutical companies are spending close to 50

billion dollars annually on the research and development of new drugs. With a return of now less than 1 approved drug per billion dollars spent, it is evident that computationally predicting strong drug candidates in early developmental stages is a critical and lucrative endeavor (11).

P450s maintain a unique and highly conserved architecture across all domains of life. Despite having relatively little sequence homology, in many cases as little as 20%, a common topological scaffold is pervasive throughout the family. The core P450 structure contains around 13 α-helices (A-L) and four β-sheets (I-IV) with the most conserved regions consisting of a four-helix bundle (D,E,I, and L) that line the active site, along with two β-sheets (I,II) that are thought to help form the hydrophobic access channel (Fig. 1.1) (12). The relative orientation of these secondary structure domains around the prosthetic heme moeity are faithfully constructed to orchestrate the heme-thiolate chemistry required for activating molecular oxygen, orientating the substrate, and binding redox partners (13). On the other hand, regions farther from the heme are found to contain more variation, and intuitively, it is these regions that are implicated in substrate recognition. Through a comparative analysis of amino acid and coding nucleotide sequences Gotoh recognized six substrate recognition sites (SRS) across mammalian and bacterial species that includes: 1) the B' Helix, 2) the C-terminal end of Helix F, 3) the N-terminal half of Helix G, 4) the N-terminal half of Helix I, (5) the β3 region and 6) a central region of β5 (Fig. 1.1) (14).

Originally discovered in 1958 in rat liver microsomes as an unknown carbon monoxide binding pigment, cytochrome P450s received their name due to the signature 450-nm optical absorbance peak when reduced and carbon monoxide bound. Five years later, the hemoprotein nature and monooxygenase function of P450s was illuminated (12). Today the main thrust of P450 research is on the human enzymes involved in xenobiotic detoxification, drug metabolism, and the biosynthesis and metabolism of lipids and steroid hormones. Yet, the enormous amount of research that has gone into the bacterial enzyme P450cam

remains primarily responsible for elucidating the remarkably powerful catalytic properties of this ubiquitous protein family.

1.3 The Putidaredoxin (Pdx)-Cytochrome P450cam (CYP101) Electron Transfer System

In the bacterium *Pseudomonas putida,* two-protein BET shuttles enable cytochrome $P450_{cam}$ (CYP101) to regio- and stereo-specifically hydroxylate *D*-camphor, its primary carbon source. This phase I biotransformation of *D*-camphor requires 2 electrons in discrete transfer events (2). An FAD-containing, NADH-dependent oxidoreductase, putidaredoxin reductase (PdR) initiates the cascade by abstracting an electron from NADH, and then a [2Fe-2S] ferredoxin putidaredoxin (Pdx), shuttles electrons between PdR and CYP101 (15). Since 1987, when CYP101 became the first P450 with a high resolution x-ray structure, it has been the paradigm for P450 structure-function studies (16), with the PdR-Pdx-CYP101 relay serving as a prototypical system for investigating the context of electron transfer between redox partner proteins in catalytic mechanisms. By 2004, all three components of the CYP101 electron transfer system had x-ray structures resolved, and more recently structures have become available for the protein partners in complex, except for one that involves the final electron transfer to CYP101 (17, 18) . Because the two electrons required for camphor catalysis are donated separately, two distinct redox environments constitute the Pdx-CYP101 interaction. The first transfer involves the reduction of the ferric Fe [III] heme in camphor bound CYP101 ($CYP101^{o}$), to the ferrous Fe [II] state ($CYP101^{r}$). After oxygen binds, another electron is transferred from Pdx^{r} to oxy-$CYP101^{r}$ which enables camphor catalysis. While CYP101's first electron can come from any agent with a suitable redox potential it is remarkably demanding in its requirement that Pdx alone donate the second electron, and be present for substrate turnover (19). It is well documented that as electrons move through the relay system of CYP101 (Fig.1.2), redox potential, as well as structural and dynamic modulation of the protein partners critically regulate redox partner

recognition. However, the enormous amount of molecular, biophysical, and kinetic data collected since early 1970s is still insufficient to explain the exact Pdx effector mechanism that couples the final electron transfer and substrate turnover events (2, 15, 20-22). Therefore, the complex structure between reduced Pdx (Pdx^r) and $CYP101^r$ is crucial to provide structural insights on this enigmatic effector activity.

1.4 Effector Mechanism in the Pdx-CYP101 complex

In the early 1970s, it was demonstrated that CYP101 did not hydroxylate camphor without the presence of its protein redox partner Pdx. Furthermore, *D*-camphor hydroxylation lost stereo-specificity resulting in substrate uncoupling and the production of superoxide anions (23, 24). The fidelity for Pdx has since been confirmed through numerous failed attempts to use strong reducing agents and homologous ferredoxins, such as adrenodoxin and terpredoxin, to complete efficient catalytic turnover (19, 21). Interestingly, cytochrome *b*5 has been identified as another competent effector for CYP101 catalysis, however it lacks the potency of Pdx, with a K_d three orders of magnitude higher (25). Pdx thus serves as an obligate effector in the substrate hydroxylation cycle of CYP101.

Two schools of thought pervade on the actual mode of effector activity. The first model espoused by the Poulos group is localized to the heme binding pocket and essentially supposes that a Pdx “push” induces structural changes which couples electron transfer and O_2 activation to proton transfer (26). This model suggests that Pdx binding on the proximal face of the heme transmits a mechanical displacement which terminates at Leu358, tilting the heme bound oxygen molecule in order to better position it for protonation by Thr252. A convincing mutagenesis study discovered that the L358P mutant spectroscopically mimics the effects of Pdx binding at the active site (27). The mutant was catalytically competent in the presence of artificial electron donors suggesting it functionally simulated the effector coupling mechanism of Pdx.

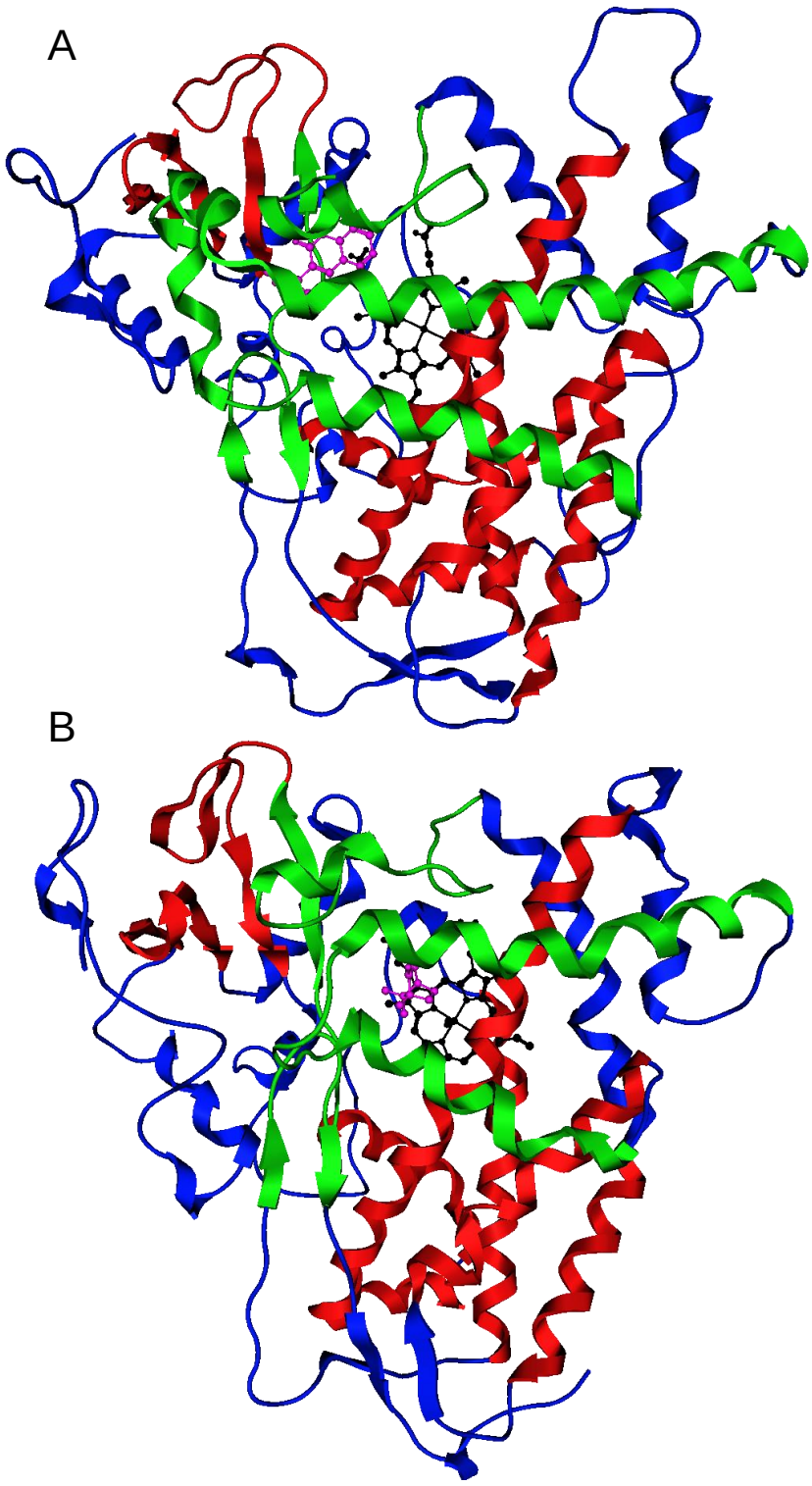

Figure 1.1.**The Conserved P450 Topological Scaffold.** Two P450s from bacterial (A, CYP101) and mammalian (B, CYP2C9) hosts showing similar overall architecture with the most conserved regions in red and the substrate recognition sites in green. The heme is shown in black and respective substrates in magenta.

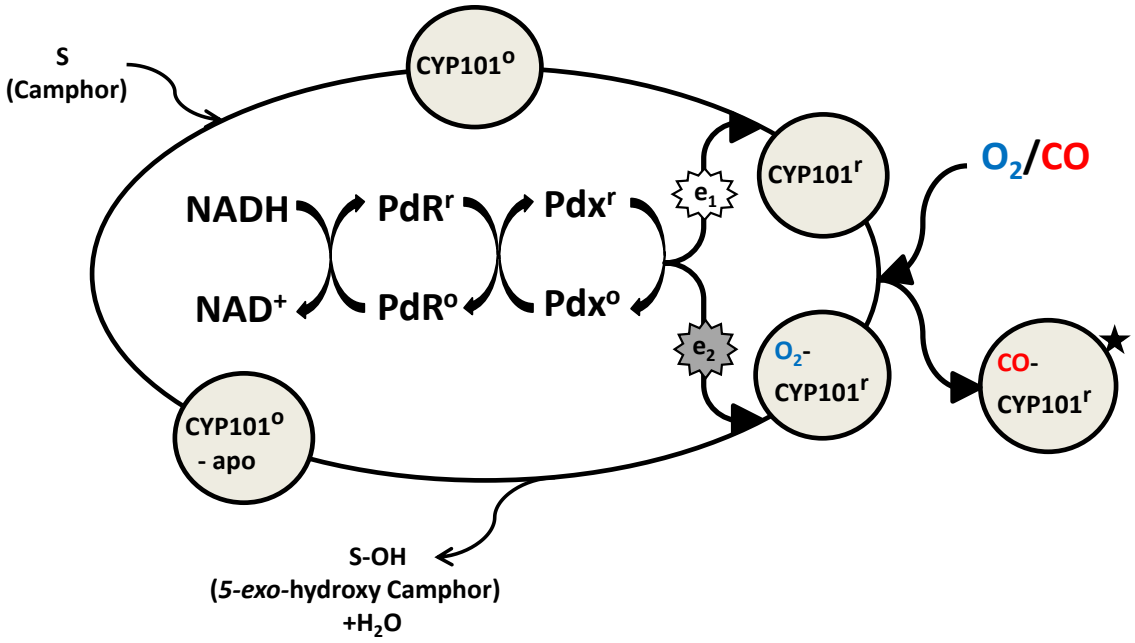

Figure 1.2. **The Biological Electron Transfer System of P450cam.** The biological electron transfer system used by cytochrome P450cam (CYP101) for catalysis of its native substrate, camphor. Putidaredoxin reductase (PdR) and putidaredoxin (Pdx) protein shuttles are shown and deliver two electrons to CYP101 in subsequent steps. The catalytic cycle of camphor hydroxylation in CYP101 is shown with the various oxidation states and ligand binding steps indicated. The effector binding step is indicated by the shaded second electron transfer from Pdx to CYP101. The kinetically trapped CO-bound CYP101 used for the reduced complex experiments in this study is indicated by ★. Pdx^r is still able to bind CO-$CYP101^r$, however no electron is transferred and it does not continue in the catalytic pathway towards camphor hydroxylation.

Crystallizing L358P highlighted further structural rearrangements in the active site (28). Here it was shown that this mutant was capable of sufficiently widening the I-helix in order to accommodate the highly ordered catalytic water molecules critical for proton shuttling and O_2 cleavage. If these changes observed in the L358P mutant faithfully emulate the Pdx-CYP101 complex, they suggest that Pdx binding couples electron transfer to substrate turnover by thermodynamically favoring the necessary conformation for O_2 activation.

The second model, championed by the Pochapsky group, broadens the scope of effector activity. In this model, it is theorized that effector binding transmits a global modulation of the conformational ensemble, effectively selecting for a subset of conformations that promote catalysis by preventing O_2 uncoupling (superoxide and hydrogen peroxide formation) and loss of substrate prior to turnover (29). Supported by a series of ^{15}N HSQC spectra with and without Pdx (and other competent effectors i.e. cytochrome b5) bound, the group identified networks of dynamic residues distal to the Pdx binding site in SRS regions, known to be critical for substrate gating, which were perturbed structurally and dynamically upon effector binding. Recently, this model was elaborated when it was shown by NMR and mutagenesis studies that Pdx binding induces a Ile88-Pro89 *trans* to *cis* isomerization event which was credited for propagating conformational changes that appropriately reorient camphor in the active site for stereospecific oxidation (30, 31). Aided by molecular dynamic simulations, it was proposed that the isomerization event initiates structural changes throughout the protein that ultimately regulate active site volume. In these simulations, the *trans* isomer conformation was shown to be 30% larger, providing evidence for how Pdx could enhance catalytic efficiency by converting CYP101 to the *cis* conformer and sterically protect against transient substrate loss (32). Collectively, this evidence compelled them to postulate that Pdx binding forces selection of a closed subset of conformations that synchronizes binding and catalysis by preventing loss of substrate prior to uncoupling. These distinct models both place Pdx effector activity within the framework of allosteric

regulation, but the first maintains a more rigid structural definition localized to a mechanical switch in the active site while the second expands the allosteric effect into globally modulated distributions of conformational populations.

1.5 Redox Modulation in the Pdx-CYP101 complex

Redox dependent structural and dynamic modulation has been observed in both CYP101 and Pdx individually (20-22, 33). Both proteins have been shown via NMR to globally attenuate their dynamic activity across all probed time regimes post-reduction (22, 33). The Pdx^{r}-$CYP101^{r}$-CO complex has a six fold stronger affinity than the Pdx^{o}-$CYP101^{o}$-O_2 complex and attenuation of dynamic amplitudes is considered a likely method of increasing the complex affinity by decreasing or prepaying the entropic cost of binding (22). In other words, reduction selects for a fraction of the conformational substates populated by the oxidized protein. A G40N mutation in the [2Fe-2S] binding loop slowed the conformational exchange process in oxidized Pdx (Pdx^{o}) adequately for detection of peak doublets by ^{15}N-^{1}H HSQC NMR. This spectroscopic method is sensitive to conformational exchange on the micro-milli second timescale, and doublets can be interpreted as distinct conformational substates in this regime. Pdx^{r} showed a degeneracy of the doublets suggesting it occupied only one of the conformational substates (21). Moreover, NMR hydrogen-deuterium exchange experiments, which monitor secondary structure motions on the milli-second and greater timescales, found slower exchange rates in $CYP101^{r}$ indicating lower-amplitude dynamics exist in the slower time regimes as well (22). Notably, the biggest differences were found in regions implicated in substrate access and Pdx binding. This evidence collectively suggests that dynamic redox regulation in the Pdx-CYP101 interaction works through a conformational selection mechanism which thermodynamically favors the distribution of populations predisposed for binding; effectively expediting the encounter complex search.

Few major rearrangements of secondary structure are observed in either Pdx or CYP101 upon reduction, and superimposing their redox crystal structures

results in RMSD values of 1.05 Å and 0.15 Å, respectively (Fig.1.3). Attenuation of dynamic amplitudes upon reduction is nevertheless concomitant with subtle structural reorganization in Pdx. According to an X-ray crystallographic study, Tyr 33 and Asp 34 initiate a Cys45-Ala46 peptide bond flip that facilitates a new, strengthened hydrogen bonding network between the sulfurs of the metal center and the surrounding amide and hydroxyl groups. It is thought that by stabilizing a tightened conformation about the shifted [2Fe-2S] metal center, Pdx constructs a distinctive structural patch with a charged ring and hydrophobic core that facilitates molecular recognition between Pdx and CYP101 (20).

Interestingly, mutagenesis studies demonstrate unique roles for specific residues on Pdx in each oxidation state (34). Differential affinity (K_d) and electron transfer (K_{ET}) effects between the ferric and ferrous binding events of Pdx mutants D38A and W106A suggest structural differences among the two redox complexes may exist. Likewise, significant NMR backbone amide spectral perturbations in residues distal to the Pdx binding interface on CYP101, considered a signature of effector activity when complexed to Pdx^r, are not witnessed to the same extent in complex with Pdx^o (35). Unique electron transfer pathways or binding sites between redox states could account for these observations, and further emphasize the importance of structurally characterizing their differences in order to elucidate the mechanism of redox modulated binding and effector activity.

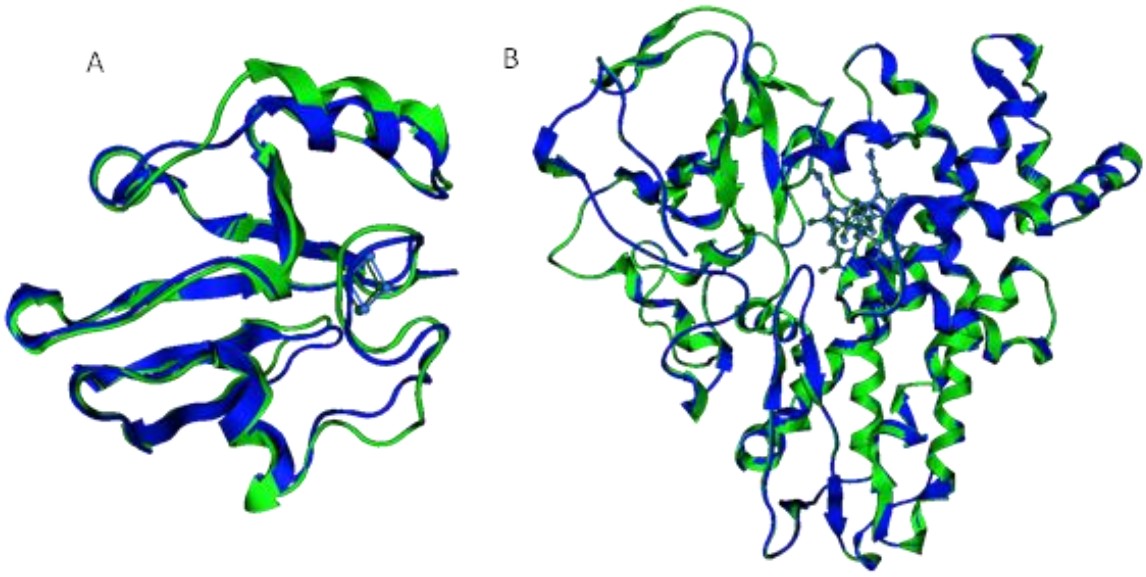

Figure 1.3.**Superimposed redox structues of Pdx and P450cam.** Superimposed NMR solution structures of a) Pdx (PDB ID: 1YJJ and 1YJI) and crystal structures of b) CYP101 (PDB ID: 2CPP and 3CPP) in the oxidized Fe [III] (green) and reduced Fe [II] (blue) states. The RMSD for the oxidized and reduced Pdx and CYP101 structures are 1.05 Å and 0.15 Å respectively.

.

Figure 1.4.**Structure of the Pdx^{o}-CYP101^{o} complex.** Cartoon representation of the solution NMR structure of the Pdx^{o}- CYP101^{o} complex determined with residual dipolar coupling (RDC) and paramagnetic relaxation enhancement (PRE) restraints by Zhang *et al*. (17).

1.6 Structure Determination of the Pdx-CYP101 Complex

While considerable kinetic, biochemical and biophysical work has been carried out over the last five decades to investigate the nature of the Pdx -CYP101 interaction, a detailed structural interpretation of the functionally relevant Pdx^r-$CYP101^r$ complex still remains elusive. The structure of this complex will likely provide significant insight on the effector activity of Pdx. However, the transient lifespan of the Pdx-CYP101 interaction, and most electron transfer protein-protein interactions, complicates co-crystallization as a means of complex structure determination. To date, the only co-crystal structures resolved for a P450-redox partner complex required chemical cross-linking (36, 37), a less physiologically relevant solution (18, 38). This method was used in the case of PdR-Pdx from the CYP101 electron transport system, as well as the AdR-Adx complex from a separate P450 system, and more recently, the Pdx-P450cam complexes in the oxidized and reduced form. However, the authors acknowledge restricting mobility of the protein partners can functionally impair the interaction as well as distort the native binding interface. Perhaps a more relevant, in solution approach for solving electron transfer complexes in fast exchange is offered by the pronounced effects of paramagnetic centers in NMR spectra (17, 39-41). The effects which manifest in NMR spectra as line shape and intensity changes offer translational information that is obtainable at long ranges. Traditional methods of protein structure determination by NMR rely on almost complete resonance assignment of the protein residues and utilize distance restraints limited to 5 Å based on the nuclear Overhauser effect (NOE). Furthermore, NOE's are confounded by line broadening and spectral overlap in large protein complexes with slow tumbling times (42). On the contrary, paramagnetic effects such as relaxation enhancement (PRE) and pseudo-contact shift (PCS) can yield resonance intensity (peak height) and chemical shift changes within 15-40 Å of the paramagnetic center (43). Due to these advantages, site-directed paramagnetic spin labeling has become an attractive approach for protein structure determination in solution.

Recently, our group solved the Pdx^{o}-$CYP01^{o}$ complex structure using NMR with a combined residual dipolar coupling (RDC) and paramagnetic relaxation enhancement (PRE) approach (Fig.1.4) (17). Yet, the more physiologically relevant redox state of the complex, where CYP101 is in a state poised to accept the second electron for substrate turnover, and Pdx exerts its effector activity, is the reduced Fe [II] state of both partners (Fig.1.2). It is difficult to trap this state due to its short-lived nature when bound to oxygen, and therefore to keep both proteins in the reduced Fe [II] state, the reaction cycle is competitively inhibited with carbon-monoxide as is often used to mimic the oxy-Fe [II] interaction (44).

To determine unequivocally if redox-dependent dynamic modulation alters the mode of binding, we have designed a NMR-based strategy to resolve the reduced complex structure employing a similar PRE/RDC methodology to the one used for the oxidized complex, albeit with some important modifications. Instead of using the conventional nitroxy MTSL paramagnetic spin label as done in the case of oxidized complex, an S-cysteaminyl-EDTA metal chelating spin label was conjugated to Pdx. This allowed for coordination of long range paramagnetic metals such as Gd^{3+} and Tb^{3+} that can tolerate reducing conditions. Additionally, an innovative photochemical reduction method was used to circumvent the problem of disulfide bond cleavage between the protein and chelating tag. Ultimately, this report provides a detailed structural interpretation of the reduced Fe [II] Pdx^{r}-$CYP101^{r}$ and the oxidized Fe [III] Pdx^{o}-$CYP101^{o}$ electron transfer complexes. Characterizing these complexes will help explain how oxidation state modulates binding to CYP101, as well as provide structural insights into how reduction enables Pdx to serve CYP101 as an allosteric effector.

CHAPTER II

CHARACTERIZATION OF REDOX-DEPENDENT CHANGES IN PDX AS A RESULT OF COMPLEX FORMATION

2.1 Protein Expression

Pdx and CYP101 were expressed and purified using methods described previously (35). Chemically competent E. Coli BL-21 cells (New England Biolabs) optimized for protein expression containing a pET or pUC expression vector (Clonetech) with a CYP101–His_6-tag fusion or Pdx protein gene insertion respectively, were inoculated into 50 mL of sterilized LB medium from 15% glycerol stocks stored at -80 ^{o}C, and allowed to grow at 37 ^{o}C with shaking at 250 rpm until the optical density at 600 nm ($O.D._{600}$) reached 0.5-0.6. The cell culture was then divided in half and 25 mL aliquots were centrifuged at 5,000 rpm for 15 min. The supernatant was discarded and the pellet was resuspended in 1 liter of defined media (M9) containing the following ingredients: 7 g Na_2HPO_4; 3.5 g KH_2PO_4; 0.5 g NaCl; 4 g L-Dextrose; 1 g NH_4Cl or unlabeled NH_4Cl; 0.102 g $MgSO_4$, 0.0057 g $FeCl_3$; 0.0165 g $CaCl_2$; 0.005 g Thiamine; and 1 mL of a Trace Elements solution containing the following in g/L: 5 Na_2EDTA; 0.5 $FeCl_3$; 0.05 $ZnCL_2$; 0.01 $CuCl_2$; 0.01 $CoCl_2.6H_2O$; 0.01 H_3BO_3; 1.6 $MnCl_2.6H_2O$. For ^{15}N isotopic labeling, $^{15}NH_4Cl$ was used instead of unlabeled NH_4Cl. Kanamycin or ampicillin antibiotics were added at a working concentration of 50 µg/mL in order to place selective pressure on the cells carrying the pET or pUC vector which carried the resistance respectively. The culture was allowed to grow until it reached an $O.D._{600}$ of 0.8- 1.0, at which point protein expression was induced with 1 mL of 0.5M Isopropyl β-D-1-thiogalactopyranoside (IPTG). Additionally, when expressing CYP101, 35 mg/L of the heme precursor, delta-aminolevulinic acid hydrochloride, was added at the point of induction to aid in maximizing heme biosynthesis for incorporation by CYP101. The cells were harvested 4-5 hrs post-induction by centrifuging at 5,000 rpm for 15 min. The supernatant was

discarded; the pellet was weighed and then stored at -80 ^{o}C for future protein extraction.

2.2 Protein Purification

For both CYP101 and Pdx, 10 g of harvested cell pellet was transferred into 50 mL of protein buffer containing the following compounds in g/L: 0.04 K_2HPO_4; 0.01 KH_2PO_4; 0.05 KCl; 0.3 camphor and resuspended via stirring until the solution was homogenized. Cell lysis was then performed by sonication. In order to separate the cell debris from the soluble intracellular components, centrifugation of the lysed cell solution was executed twice at 13,000 rpm for 15 min and the supernatant saved from each run. At this point, the reducing agent, dithiothreitol (DTT) was added at 1 mM concentration to increase protein stability. The crude CYP101 supernatant was passed through a cobalt metal affinity column (Talon Metal Affinity Resin, Clontech Laboratories) for the purposes of capturing CYP101 via the His_6-tag. Subsequently, the cobalt column was washed with 50 mL of protein buffer to help reduce non-specific binding. CYP101 was then eluted with 5 0mL of protein buffer containing 125 mM imidazole. The Pdx purification, as also the next step in CYP101 purification, began by passing the protein solution through an anion exchange Q Sepharose Fast Flow column (GE Healthcare Lifesciences). With either protein bound to the resin, 50 mL of buffer was passed over the anion exchange column to reduce non-specific binding before the protein was eluted by increasing the KCl concentration to 300 mM. Either protein was then concentrated using Amicon Ultra centrifugal filters (Millipore, 10,000 MW) before final purification using size exclusion chromatography performed on an AKTA FPLC system. The concentration of CYP101 or Pdx was calculated through Eq. (2)

$$A_{391} \text{or} A_{325} = \varepsilon \beta c \qquad (2)$$

where A = the absorption intensity at the characteristic wavelength (391 nm for CYP101 and 325 nm for Pdx), ε= the molar extinction coefficient in mM^{-1} cm^{-1}, β = path length of the cuvette (1 cm), and c = concentration in mM. The protein was considered >95% pure when the ratio of A_{391}/A_{280} or A_{325}/A_{280} exceeded 1.4 or 0.6 for CYP101 and Pdx respectively (29). The protein samples were then concentrated using Amicon Ultra centrifugal filters (Millipore, 10,000 MW) and their final concentration measured as described above before being used for NMR experiments.

2.3 Redox-Dependent Changes in Pdx monitored by solution NMR spectroscopy

A number of studies have demonstrated that oxidation state influences the binding of Pdx to CYP101; yet to date, no exhaustive characterization of the redox-dependent NMR spectral changes arising in Pdx^r upon complexation with $CYP101^r$ has been reported. Heteronuclear NMR is an effective way of qualitatively monitoring structural and dynamic changes quickly between various conditions. Standard ^{15}N-^{1}H HSQC spectra capture a resonance “fingerprint” of the protein backbone that provides both chemical shift, δ (structural) and linewidth, λ (dynamic) observables at single residue resolution (45). Chemical shift or resonance frequency is a reflection of the chemical environment of atomic nuclei, and therefore changes in chemical shift Δδ between different conditions provide insight into structural perturbations. Linewidth (λ), or width of a peak at half height, is a second observable present in ^{15}N-^{1}H HSQC spectra which contains information on the dynamics of the residue over the micro to millisecond time regimes. Since λ receives contributions from dynamic activity over a broad range of timescales, and little correlation has been established between the magnitude and direction of Δδ with the nature of the structural change, only qualitative inference can be made concerning the rate of change between various time regimes and the conformational modification (45).

To initially probe if Pdx effector activity and/or binding to CYP101 is redox dependent, and confirm consistency between this and previous investigations, ^{15}N-^{1}H HSQC spectra were collected at 30^{o}Cfor Pdx in both its Fe [III] and Fe [II] oxidation states. ^{15}N-^{1}H HSQC spectra were also collected, for Pdx^{o} in complex with CYP101^{o} and Pdx^{r} in complex with CYP101^{r}, at a 1:2 molar ratio of Pdx:CYP101, with a final Pdx concentration of 50 µM. Of the 106 residues in Pdx, assignments are available for 78 backbone amides as well as side chain assignments for Trp106 and Arg83. Resonance assignments for CYP101^{r}, Cyp101^{o} and Pdx^{o} were obtained from the Biological Magnetic Resonance Bank (BMRB) managed by the University of Wisconsin at www.bmrb.wisc.edu with the accession numbers 5759, 17415, and 4154 respectively. Due to the paramagnetism of Fe [III] and Fe [II] in the [2Fe-2S] metal cluster, residues within 8 Å of the Fe-S metal center are severely broadened and largely unassigned in both redox states. Pochapsky's group has previously reported the redox-dependent spectral changes in Pdx and CYP101 alone, as well as the changes occurring in CYP101^{r} in complex with Pdx^{r} (21, 29, 33). Here we detail the spectral changes in Pdx^{r} as a result of CYP101^{r} binding. Additionally, titrations of Pdx were conducted with CYP101 in both oxidation states to calculate dissociation constant (K_d) values as a prelude to the complex structure determination.

To deconvolute the changes occurring either due to reduction or binding to CYP101, spectral comparisons of Pdx were done under each condition. Specifically, ^{15}N-^{1}H HSQC spectra were collected for Pdx in both oxidized and reduced states first. Redox-dependent spectral changes for Pdx observed in these spectra are mostly similar to those reported previously by Lyons *et al* (33), except for a few differences. The chemical shift and line broadening profiles of in our spectra agree well with the ones reported by Lyons *et al*. with the largest spectral changes occurring between residues 27-29 of Helix D, 71-78 of Helix G, and residues 104-106 at the C-terminus. Other changes were also noted which went unreported in the earlier studies. This could be a result of additional

resonance assignments since the original study as also a more detailed analysis of the observed spectral changes. Interestingly, some of the newly observed changes were for residues that may have functional significance. For example, Asp 34 was found to have a drastic upfield shift in its ^{15}N resonance along with a more moderate upfield shift in Tyr33. This difference is particularly notable in light of an X-ray crystallography study on the redox-dependent structural reorganization of Pdx which suggested that Tyr 33 and Asp34 transmit the redox signal by initiating a reconfiguration of the hydrogen bonding networks throughout the protein (20). Furthermore, certain other residues that were previously reported to broaden beyond detection (e.g. Leu71), were now observed, perhaps due to increased sensitivity of peaks in our spectra. On the other hand, resonances for several residues that were previously reported broadened beyond detection following reduction were also broadened out in our experiments including those for Leu23, Val50, Met70, and Ile88 (Fig. 2.1 a and b). The similarity of results suggests that our experimental methodology is consistent with that employed previously by other groups.

Binding studies of Pdx with CYP101 in each oxidation state were performed next to map redox-dependent spectral changes in Pdx upon complexation with CYP101. An interesting observation made from these experiments was that many of the same residues in Pdx perturbed here as a function of oxidation state are also perturbed in the complex between Pdx and CYP101, and are likely present at the complex interface (17). In a previous study which studied the oxidized complex by NMR, the most dramatic changes taking place for backbone amide resonances were reported at residues 28-32 (helix D) and 104-106 (C-terminus) in Pdx, which are the same regions that are also affected in a redox-dependent manner. The spectral changes found in our investigation of the oxidized complex are generally in good agreement with those reported earlier (Fig.2.2a and 2.2b) (17). Therefore, consistency and reproducibility with previous data allowed us to perform an accurate comparison of the spectral differences in Pdx within the reduced and oxidized complex.

Differences in chemical shift perturbations for Pdx between the oxidized and reduced complexes were observed at all three experimentally accessible interfacial regions, Helix D, Helix G, and the C-terminus (Fig.2.2c). In addition to these differences, resonances for backbone residues on helix G (71 and 74) and the C-terminal Trp106 were severely broadened or disappeared completely in the reduced complex (Fig.2.2d) which suggests a change in the dynamic properties for these residues. Interestingly, Asp34 which was suggested as the structural switch in H-bond re-networking, as well as other residues shown via X-ray crystallography (7-9, 33-35) to partake in the new H-bond network, exhibit significantly different resonance frequencies (Fig.2.1a and 2.1b). Taken together, this data corroborates the redox-dependent conformational dynamics model where Pdx reduction selects for a tightened conformational subset where residues at the docking interface are likely rearranged and better positioned for binding with CYP101, making it feasible for them to form differential contacts compared to the oxidized complex. However, in line with the dynamic model, it is also possible that changes in the reduced complex are more intense simply as a result of tighter binding with dynamically attenuated CYP101 (Fig. 2.2c and 2.2d).

.

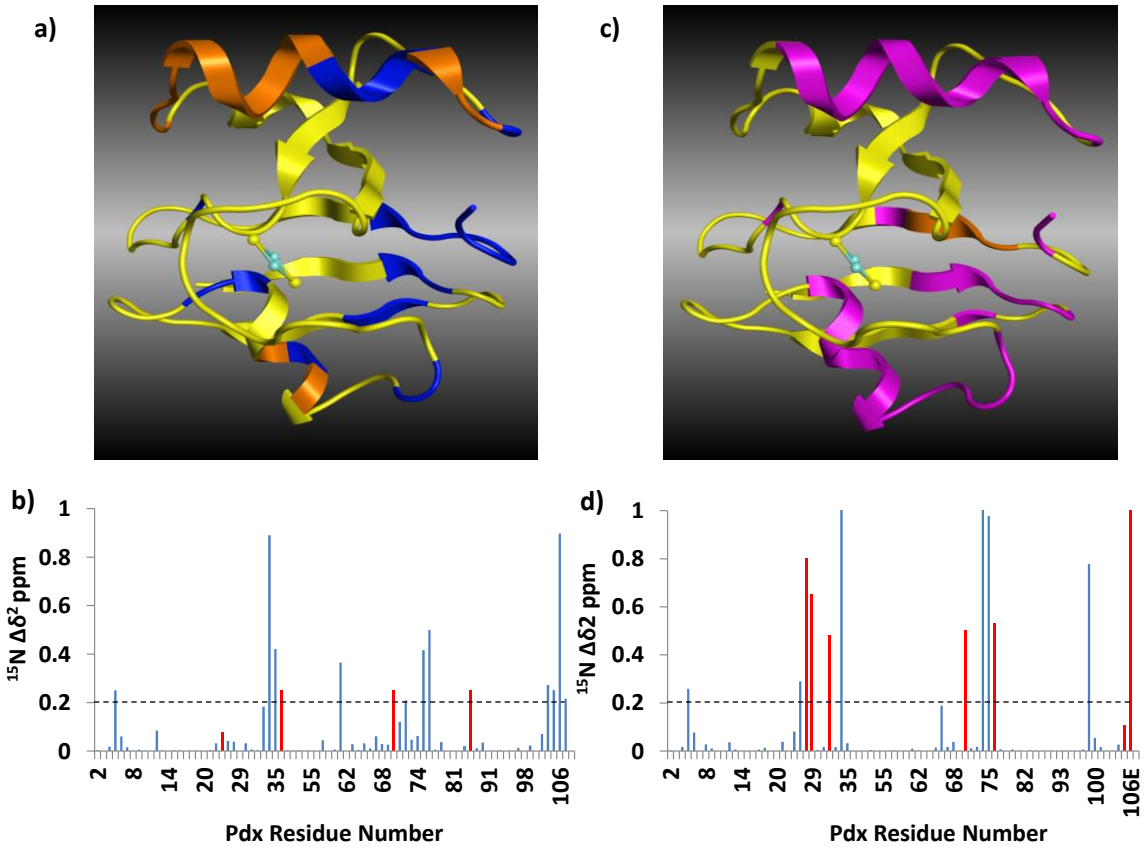

Figure 2.1. **Spectral Changes for Pdx upon reduction and CYP101 binding**. ^{15}N-^{1}H spectral changes observed for Pdx upon reduction [a) and b)]; and in response to CYP101^{r}binding [c) and d)]. Cartoon representations of the Pdx backbone from the perspective of the CYP101 binding interface are color coded to show distribution of secondary structural features perturbed. Dotted lines represent threshold cutoff for large vs. small changes. a) Large spectral changes between Pdx^{o} and Pdx^{r} are shown in blue, while smaller changes are shown in orange; b) ^{15}N chemical shift changes Δδ = (Pdx^{o}-Pdx^{r})^{2} plotted versus residue number in Pdx. Red bars indicate severe or complete broadening for that residue; c) Large spectral changes between Pdx^{r} and Pdx^{r}-CYP101^{r} are shown in magenta, whereas smaller changes are shown in orange; d) ^{15}N chemical shift changes Δδ = (δPdx^{r}-δPdx^{r}-CYP101^{r})^{2} plotted versus residue number in Pdx. Red bars indicate severe or complete broadening for that residue.

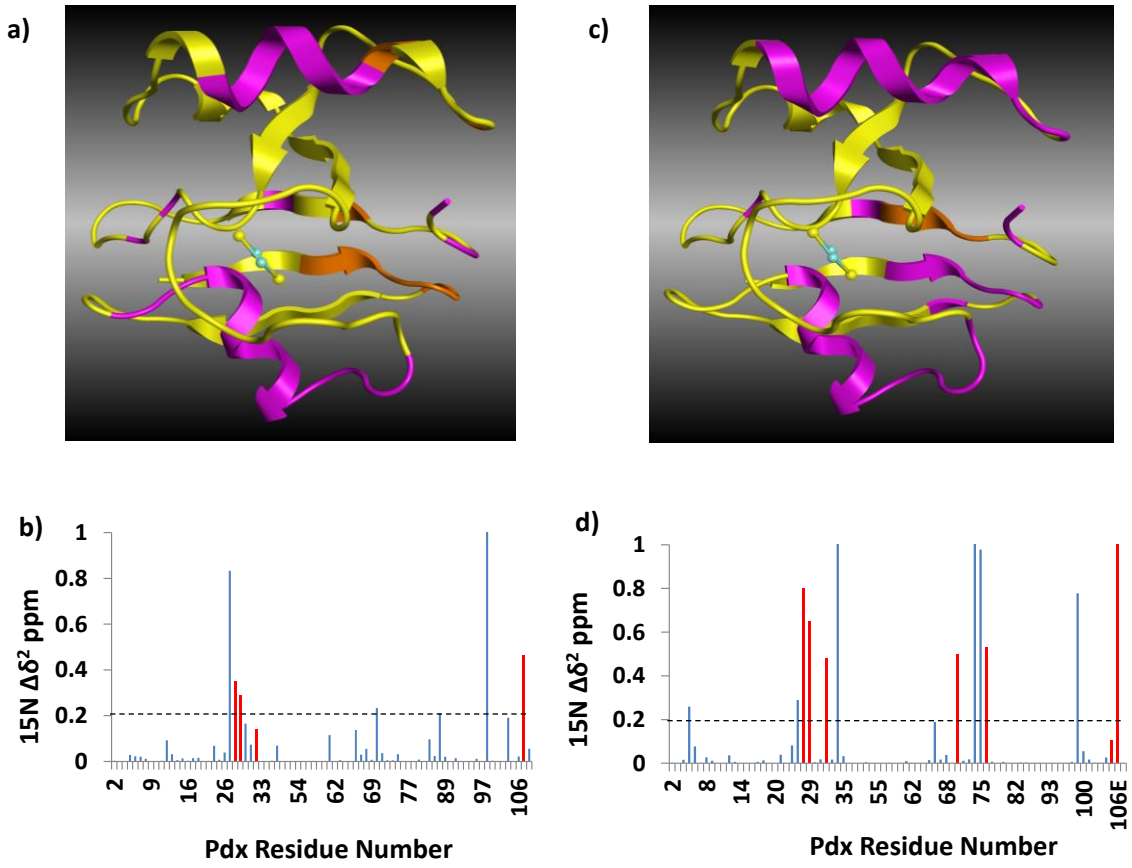

Figure 2.2. **Spectral Changes for Pdx upon Binding CYP101 in each Redox State.** ^{15}N-^{1}H spectral changes observed for Pdx^{o} upon binding CYP101^{o} [a) and b)]; for Pdx^{r} binding to CYP101^{r} [c) and d)]. Cartoon representations of the Pdx backbone from the perspective of the CYP101 binding interface are color coded to show distribution of secondary structural features perturbed. Dotted lines represent threshold cutoff for large vs. small changes. a) Large spectral changes between Pdx^{o} and Pdx^{o}-CYP101^{o} are shown in magenta, whereas smaller changes are shown in orange; d) ^{15}Nchemical shift changes $\Delta\delta = (\delta Pdx^{r}-\delta Pdx^{r}\text{-}CYP101^{r})^{2}$ plotted versus residue number in Pdx. Red bars indicate severe or complete broadening for that residue; c) Large spectral changes between Pdx^{r} and Pdx^{r}-CYP101^{r} are shown in magenta, whereas smaller changes are shown in orange; d) ^{15}Nchemical shift changes $\Delta\delta = (\delta Pdx^{r}-\delta Pdx^{r}\text{-}CYP101^{r})^{2}$ plotted versus residue number in Pdx. Red bars indicate severe or complete broadening for that residue.

2.4 Titrations of CYP101^{r}and CYP101^{o} with Pdx^{r} and Pdx^{o} for estimation of binding affinity (K_d values) in the redox complexes

As a prelude to structure determination of the oxidized and reduced complexes, it is important to characterize the relative affinity of the complexes which would facilitate structural data analysis of the complexes. Thus, binding affinities in the form of K_d values were estimated for the oxidized and reduced complexes under the experimental conditions identical to those employed for structural measurements. A series of seven ^{15}N, ^{1}H TROSY-HSQC spectra were acquired to follow the chemical shift perturbations of NH coupled pairs in CYP101 during titrations of Pdx^{r} and Pdx^{o} with CYP101^{r} and CYP101^{o}, respectively. In each oxidation state, titrations were conducted at 25^{0} C in 40 mM TRIS-HCl buffer (pH 8.0) containing 40 mM KCl with a final CYP101 concentration of 50 µM. Aliquots of Pdx in the same buffer were added to yield final molar ratios (Pdx/CYP101) of: 0, 0.25, 0.5, 0.75, 1, 2 and 3. Measuring the change in Hz for ^{1}H chemical shifts δ during titrations, allowed for estimation of the dissociation constant (K_d) for the complex in each oxidation state using Eq.(3):

$$\delta = \delta_0 + (\delta_{max} - \delta_o)\left\{K_d + m_o + p_o - [(K_d + m_o + p_o)^2 - 4m_o p_o]^{1/2}\right\}/2m_o \qquad (3)$$

where δ_0 and δ_{max} are the chemical shifts of the free and saturated forms of CYP101 respectively, and m_o and p_o are the nominal concentrations of CYP101 and Pdx, respectively (46). Kd and δ_{max} values were estimated using the non-linear regression analysis software SigmaPlot. Five well resolved ^{15}N-^{1}H resonances were monitored in both redox complexes and the $^{1}H\delta$ versus protein concentration fits yielded values for δ_{max} and K_d. Accurate modeling of the distance restraints requires knowledge of the free and bound fractions of protein alone and in complex. Calculation of the concentration of free and bound protein fractions was accomplished with Eq. (4) (46):

$$\delta_o = X_f\delta_f + X_b\delta_b \quad (4)$$

where δ_o is the observed chemical shift at a particular molar ratio, $\delta_f$is the chemical shift in complete absence of ligand, δ_b is the chemical shift completely saturated with ligand, and X_f and X_b are the percentage of protein free and bound respectively. Using the above equation, the bound fraction of CYP101 was estimated to be ~60% and ~70% in the oxidized and reduced complexes respectively, assuming a 1:1 ratio of Pdx:CYP101.

Titrations of $CYP101^o$ and $CYP101^r$ with Pdx^o and Pdx^r, respectively yielded sequential chemical shift changes until CYP101 was considered saturated (Fig.2.3). Non-linear fits of δ as a function of Pdx^o and Pdx^r concentration for the five selected resonances yielded K_d values 24.3 ± 12 μM and 9.9 ± 5 μM for the oxidized and reduced complexes, respectively (Fig.2.4). While these values are in reasonable agreement with literature values published previously and correctly denote a higher affinity for the reduced complex; the magnitude of the affinity difference between the oxidized and reduced complex is lower than expected. Whereas a ~2.5 fold change in binding affinity is reported here, other groups reported ~6 fold change (1). This could be due to variations in the experimental buffer conditions between the two studies, or the unreliability of randomly selecting peaks as metric for binding affinity. Whether or not these differential binding affinities are responsible for the chemical shift and broadening profile differences observed between the two redox complexes is difficult to determine, and this possibility, although unlikely, cannot be ruled out.

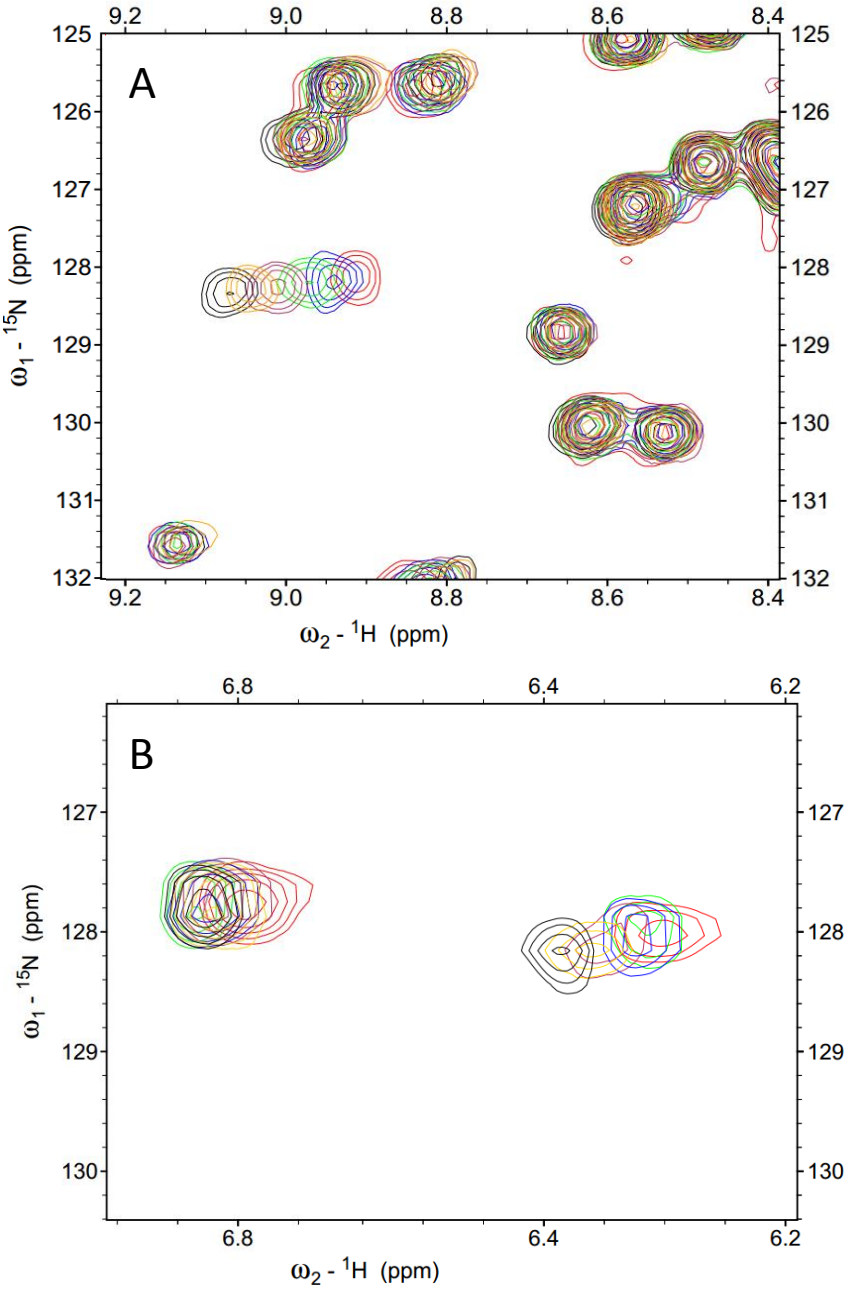

Figure 2.3. **Titration of Pdx with CYP101 to determine K_d values.** Overlay of representative peaks in the ^{15}N-^{1}H TROSY spectra for CYP101 when titrated with Pdx. A) CYP101^o titrated with Pdx^o and B) CYP101^r titrated with Pdx^r. Titration experiments were used to determine binding affinities (K_d values) for the oxidized and reduced complex. The peaks are color coded based on Pdx:CYP101 molar ratios present in each titration: 0.0 (red), 0.25 (blue), 0.5 (green),1.0 (maroon), 2.0 (gold), and 3.0 (black).

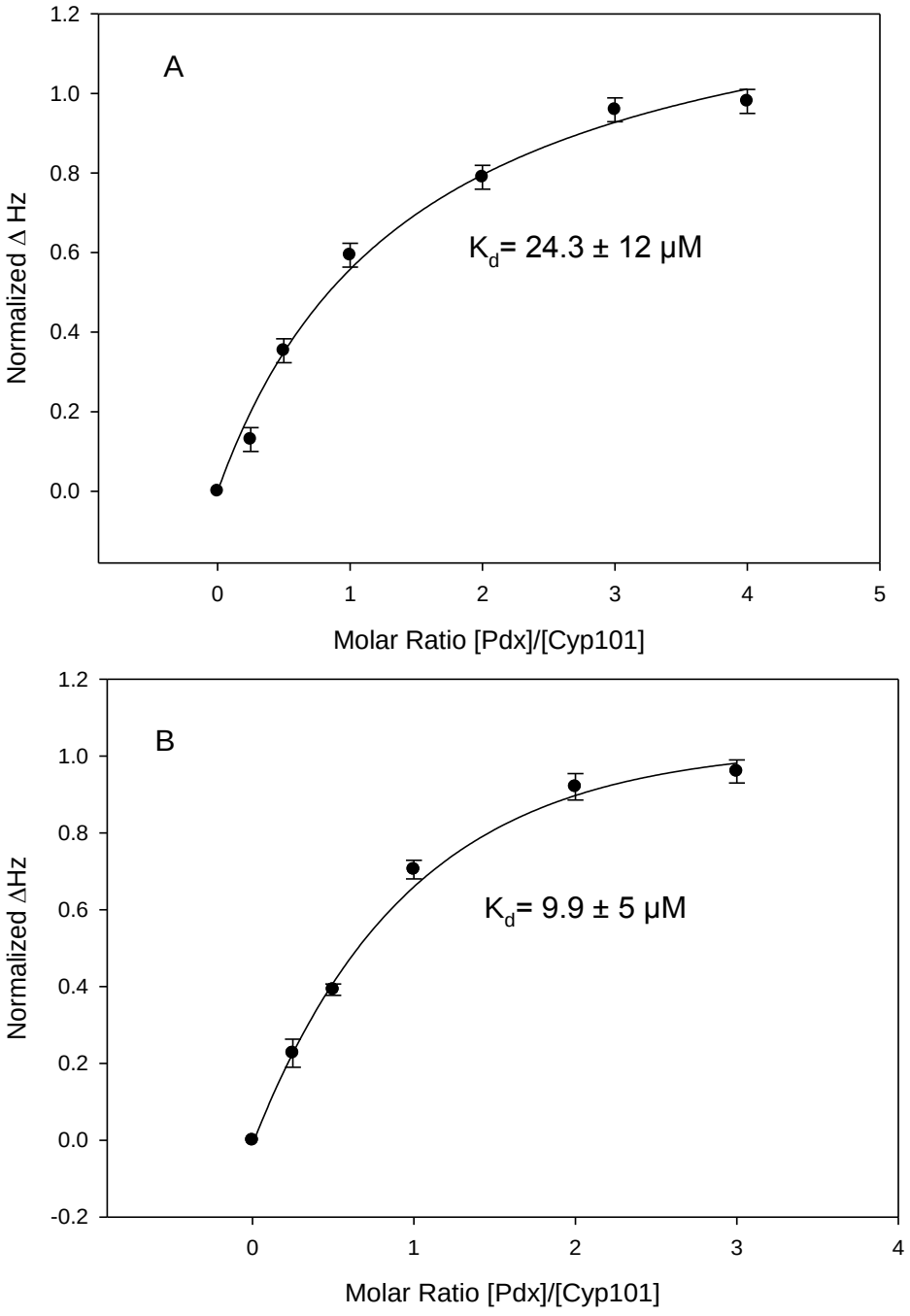

Figure 2.4.**Fitting of K_d values to the titration data in oxidized and reduced Pdx-CYP101 Complex.** Plot of normalized chemical shift perturbations as a fraction of δ_{max} for amide resonances in A) CYP101^{o}and B) CYP101^{r} as a function of Pdx^{r}and Pdx^{o} titrant concentrations respectively. Dissociation constant (K_d) values of 9.9± 5 μM and 24.3± 12 μM were calculated for the reduced and oxidized complexes respectively.

CHAPTER III
SPIN LABELING AND REDUCTION METHODOLOGIES FOR PARAMAGNETIC STUDIES

3.1 Use of Paramagnetic spin labels in protein NMR structural studies

Paramagnetic spin labeling is quickly becoming a method of choice for protein structural studies. Traditional NMR structural methods such as nuclear Overhauser effect and scalar couplings rely on interactions over a very short range (5 Å), and consequently have difficulty relating structural elements at distant sites (43, 47). Because these methods rely on near complete resonance assignments, their shortcomings are magnified in large proteins or protein complexes where peak overlap makes complete resonance assignment nearly impossible. Therefore, these methodologies remain insufficient for resolving protein structures in a timely manner. The pronounced effect of paramagnetism on surrounding nuclear spins, and hence NMR observables, offer a promising alternative for NMR structure studies. Originating at an unpaired electron, with a magnetic moment almost three orders of magnitude larger than protons, the paramagnetic effects operate over long distances, and can be exploited for translational restraints (48). It is critical that the unpaired electron be provided by an inert molecule that remains stable under biological conditions. Certain organic radicals, most frequently nitroxides, and a bevy of metal ions such as Mn^{2+}, Fe^{2+}, Cu^{2+}, Ti^{3+}, Ni^{2+}, Co^{2+}, and lanthanides, offer these unpaired electrons and are well suited for protein NMR investigation.

Several paramagnetic effect-based strategies have been developed into methods for protein NMR structural studies including: paragmagnetic relaxation enhancement (PRE) for distance restraints, as well as, pseudo-contact shifts (PCS) for both distance and orientational constraints. In PRE, nuclear-electron coupling enhances nuclear relaxation rates R_1 and R_2 in an r^{-6} distance dependent manner (Eq.6). As a result peak intensities are attenuated by

increasing linewidths (λ) according to $\lambda = 2R_2$. PCS confers both peak intensity and chemical shift changes that rely again on the distance, but also on orientation of the paramagnetic center in relation to the target nuclei. In the presence of paramagnetic metals with fast relaxing electron spins, PCS modifies spectrum observables in accordance with an r^{-3} distance dependence, as well as the polar coordinates of the nuclear spin r, θ, φ with respect to the anisotropic magnetic susceptibility tensor ($\Delta\chi$ tensor) (43, 48).

As a result of numerous physiologically relevant metal ions having paramagnetic properties, native paramagnetic centers are frequently found in the structures of metal binding or metalloproteins, and have been exploited in NMR experiments for structure elucidation (41, 49). The paramagnetic Fe [III] iron in the heme prosthetic group of CYP101 only has an influential sphere of ~8 Å, prohibiting sufficient distance restraints for complex studies. Therefore, a non-native paramagnetic spin label must be introduced on the surface of Pdx to investigate the Pdx-CYP101 complex.

Conjugation of a site directed spin label is garnering more attention as a method of expanding the application of paramagnetic structural studies to a larger number of proteins and protein complexes (41, 50). Thiol-based spin labeling utilizing disulfide chemistry is the most commonly employed conjugation technique as cysteine is the only amino acid able to participate in these reactions (51).

During the structure determination process of the oxidized $CYP101^{o}$-Pdx^{o} complex, a conventional nitroxy spin label in the form of MTSL was conjugated to Cys73 on Pdx. Its use in the reduced complex environment is precluded by the fact that the paramagnetism of nitroxy and other common spin labels can easily be lost through reduction of its unpaired electron. An added complication is the fact that the disulfide bond conjugation is also susceptible to reduction cleavage. Consequently, to utilize the paramagnetic labeling strategy in both oxidation states of the Pdx-CYP101 complex, we had to address each of these problems.

3.2 Site Specific Labeling of Pdx with Metal Chelator tag

The S-cysteaminyl-EDTA metal chelating tag, capable of conjugating to the same lone, surface exposed Cys73 on Pdx, offers an alternative to the nitroxy spin label since it is not inherently paramagnetic but rather becomes paramagnetic upon the coordination of a variety of paramagnetic metal ions. Multiple advantages are derived from metal chelater spin labels compared to traditional nitroxy ones (52), but most importantly for the aims of this study; the variety of different metals with unique paramagnetic properties offered a suite of paramagnetic centers capable of resisting reduction, and inert with respect to biological systems.

Generally following the procedures described by Pintacuda et al. (2004) and Gaponenko et al. (2002), a thiol-reactive EDTA moiety was introduced at the lone, native, solvent exposed cysteine (Cys73) on Pdx (52, 53). Pretreatment of Pdx with 1mM DTT was necessary for reducing all free cysteine thiol groups. Following this preparation, the sample was extensively dialyzed with 40 mM Tris buffer (pH 8.0) containing 40 mM KCl using an Amicon Ultra centrifugal filter (Millipore, 10,000 MW) to remove any excess DTT. Removing all of the DTT through extensive dialysis was critical for high-yield derivations. Subsequently, S-(2-pyridylthio)-cysteaminyl-EDTA (Toronto Research Chemicals) was added to the protein solution at ten-fold excess and allowed to incubate overnight in the dark at 4 ^{o}C. Excess label and by-products were removed by dialysis prior to conjugation verification or metal addition. ^{1}H-^{15}N HSQC NMR analysis of ^{15}N labeled Pdx revealed that >95% of the protein was modified without any major structural perturbations. Minor chemical shift changes occurred for 5 residues including C73 that did not exceed 0.15 ppm in either dimension of the HSQC spectrum, suggesting the native protein conformation remained intact (Fig.3.1). Different metal salts ($GdCl_3$, $MnCl_2$, and $TbCl_3$) were coordinated to EDTA-conjugated Pdx by adding them at 1.25 times the protein concentration to initiate metal coordination to the EDTA site on S-cysteaminyl-EDTA-conjugated Pdx (Pdx-EDTA). Uncoordinated metal ions were then removed through extensive

dialysis with 40 mM Tris buffer containing 40 mM KCl and 2 mM camphor. Metal ions such as Gd^{3+} and Mn^{2+} were used to coordinate the EDTA tag for quantitative PRE measurements, since they don't have fast relaxing electrons which can cause undesirable pseudocontact shifts in addition to broadening of resonances.

Conjugating Pdx with the EDTA spin label at Cys73 should not impair the ability of Pdx to form native complex with CYP101 in either oxidation state since it did not significantly alter the structure of Pdx as evidenced by marginal changes in the chemical shifts of the resonances in Pdx. Furthermore, Cys73 while being actively involved in Pdx docking to PdR, has little to no role in the Pdx-CYP101 interaction (54) and therefore, in our opinion, modification of this residue does not compromise the formation of a physiologically relevant complex between CYP101 and Pdx. The structures for both oxidized and reduced complexes determined using the spin label methodology here should provide a faithful representation of these structures in solution.

3.3 Photochemical Reduction of CYP101 and Pdx

Sodium dithionite is a well-established reducing agent for Fe-based electron transfer metalloproteins (55). It and other established protein reducing agents (i.e. chromosulfate, DTT, beta-mercaptoethanol) all operate via a sulfur-based moiety which for our purposes was an impediment to EDTA spin label derivation. Finding an agent/s with sufficient redox potential for Pdx and CYP101 reduction, with minimal pH effects, and one that is also inert with respect to disulfide bonds was a formidable challenge. While using the native BET protein shuttle pathway from from PdR to Pdx to CYP101 remained an option, it was considered a last resort due to the detriments of protein instability, slower ET rates, and a crowded protein environment. Fortuitously, some data was available on a photosensitizing proflavine based synthetic pigment system that was capable of photochemically initiating electron relay in the P450cam system (56).

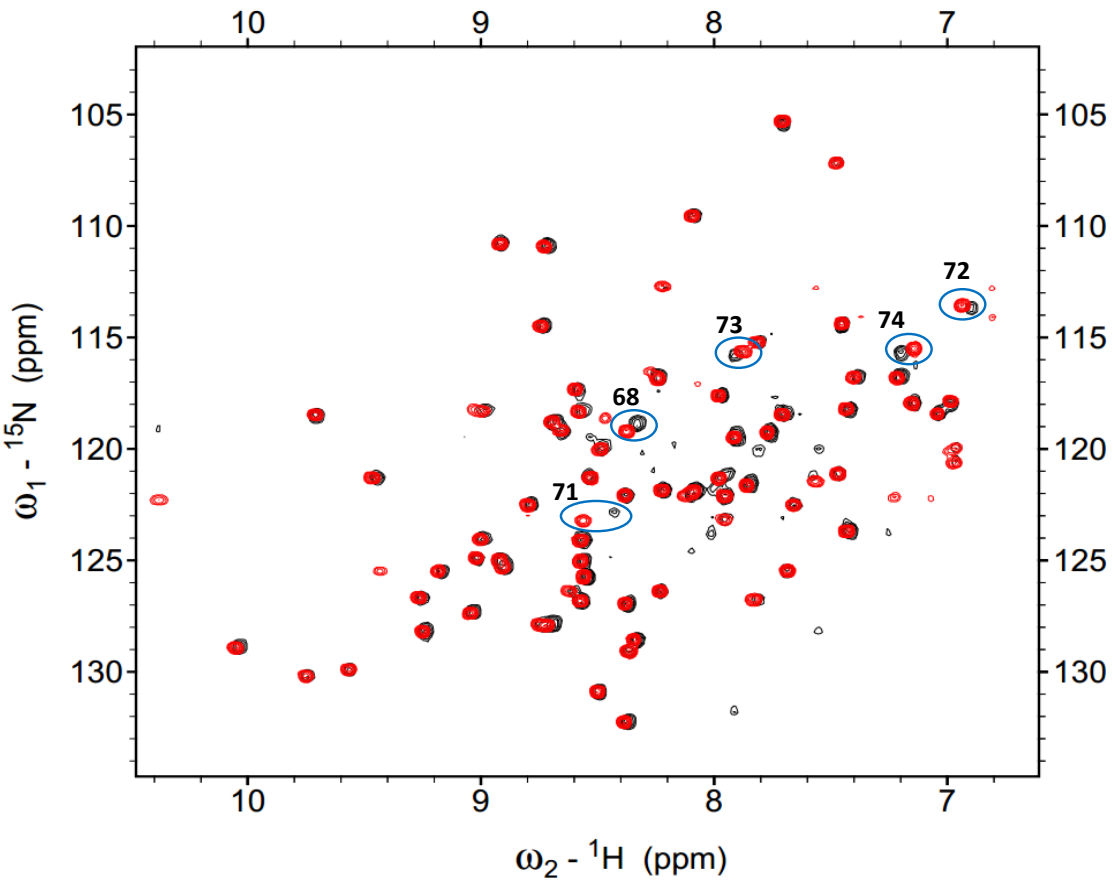

Figure 3.1. **Spectral Changes in Pdx^{o} upon EDTA Spin Label Conjugation.** Overlay of ^{15}N-^{1}H HSQC spectra of Pdx^{o} with (black) and without (red) the EDTA metal chelating label conjugated to Cys 73. Blue circles indicate the 5 peaks with their corresponding residue assignment that are perturbed consistently upon conjugation.

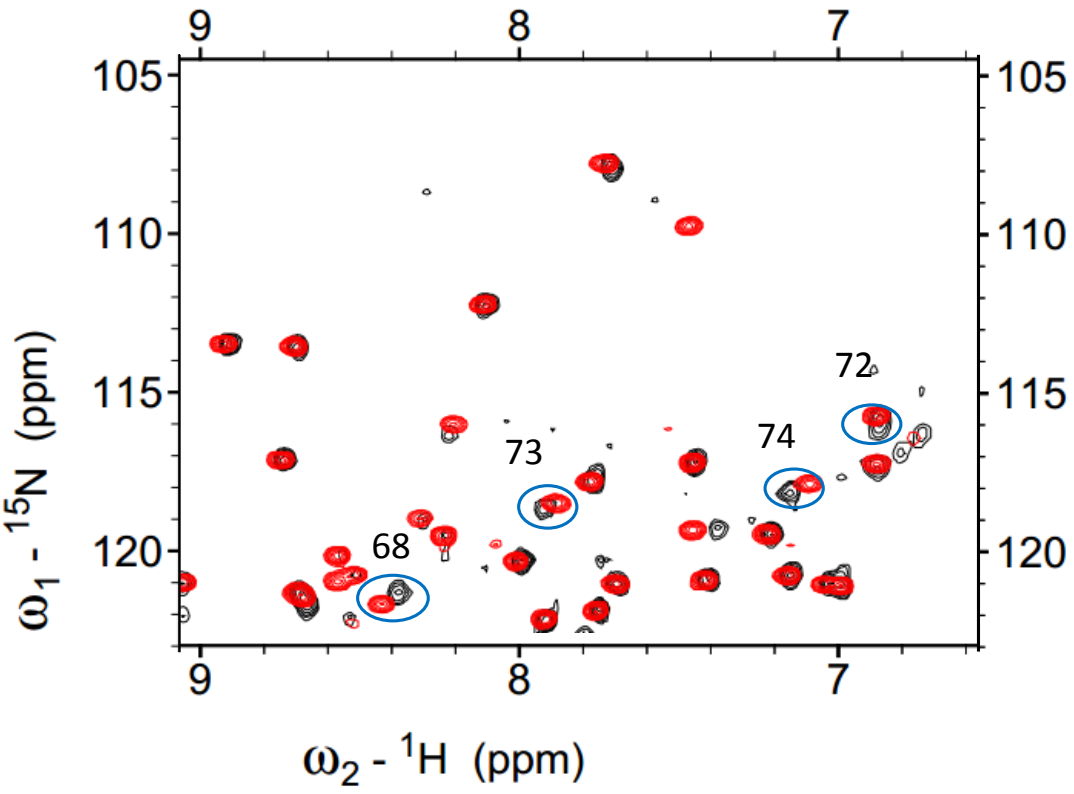

Figure 3.2.**Spectral changes in Pdx after spin label conjugation and reduction.** Overlay of ^{15}N-^{1}H HSQC spectra of Pdx^r with (black) and without (red) the EDTA metal chelating label conjugated to Cys73. The same resonances perturbed in the oxidized spectra were also perturbed post-reduction indicating that reduction did not affect the stability of the conjugation.

After extensive testing and optimization, this method was employed to reduce Pdx tagged with the EDTA metal chelator as well as CYP101.

Reduced CO-bound CYP101-Pdx samples were prepared in the following manner - A method outlined by Greenbaum, which describes using a synthetic pigment system electron donor as alternative pathway to the endogenous putidaredoxin reductase (PdR), was a guideline for our reduction (56). In 3 separate 4 mL vials; H_2O with 2 mM camphor, pure D_2O, and a photochemical stock containing: 100 µM proflavine (MP Biomedicals), 2 mM methylviologen (ACROS Organics), and 10 mM NADH (Research Products International) were degassed by N_2 gas purging for at least 1 hr. Pdx and CYP101 samples were degassed separately in 4 mL vials by layering N_2 for a minimum of 2 hr. Each protein sample consisted of 150 µL of protein at 0.1 mM concentration and combined to obtain a final NMR volume of 300 µL and a final protein concentration of 0.05 mM. Carbon monoxide (CO) was dissolved into degassed H_2O by purging for at least 15 minutes and then layered over the degassed CYP101 solution for an additional five minutes. All vials were sealed with parafilm and transferred to an anaerobic chamber where the components were mixed. 25 µL of the photochemical pigment stock and 10 µL of D_2O were added to both the Pdx and CYP101 solutions. The CYP101 and Pdx protein solutions were then mixed before using the 2 mM camphor H_2O stock to bring the final volume to 300 µL. The final sample was anaerobically transferred to the NMR sample tube (Shigemi), and the NMR tube sealed. Placing the NMR sample under a generic fluorescent, 1500 lumen white light initiated the electron transfer by photosensitization of proflavine. After 10 minutes of irradiation, the sample visibly appeared blue and the proteins were assumed to be completely reduced. Reduction of methyl viologen results in a blue-shift, which allowed us to visibly monitor loss of oxygen availability, indicating a fully reduced environment in the sample.

Comparing the ^{15}N-^{1}H Pdx spectral differences between conjugation and reduction conditions allowed us to determine unequivocally that photochemical

reduction did not interfere with spin labeling (Fig.3.2), unlike results from sodium dithionite reduction. In addition to not cleaving disulfide bonds, the proflavine based synthetic pigment electron relay system was considerably less detrimental to the protein compared with dithionite, most likely due to its advanced oxygen scavenging capacity and subdued pH effects. Stability assays confirmed CYP101 was stably reduced for over 56 hrs (data not shown). Superimposing the ^{15}N-^{1}H HSQC-TROSY spectrum of $CYP101^{r}$ reduced by the traditional reducing agent sodium dithionite and with that of CYP101 reduced by the photochemical reduction system illustrates that no significant differences exist between the two reduced structures (Fig.3.3). Ultimately, the conditions imposed here including: the paramagnetic label derivation, metal coordination, and photochemical reduction are unlikely to alter a faithful representation of the native interaction between CO-$CYP101^{r}$-Pdx^{r}.

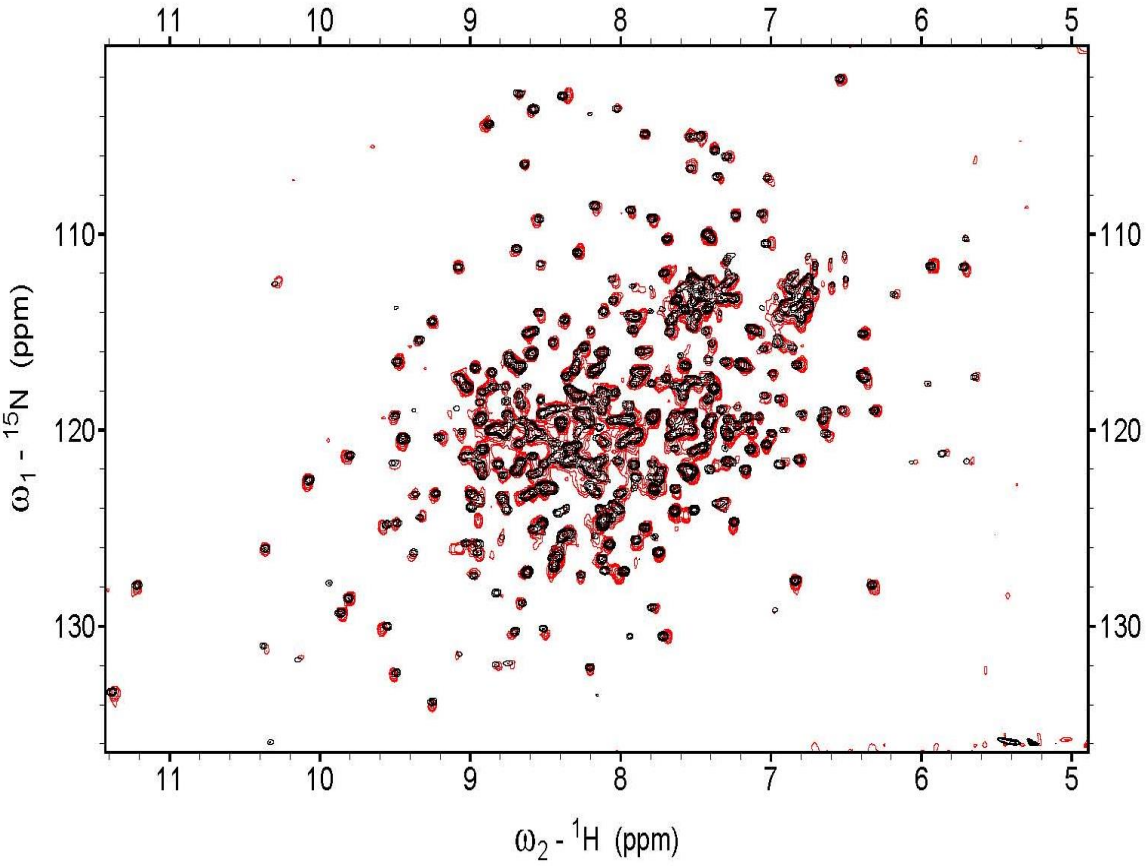

Figure 3.3. **Spectral Comparison of Photochemical and Dithionite Reduction methods.** Superimposed ^{15}N-^{1}H spectra of CO-bound CYP101^{r} reduced with methylviologen (red) and sodium dithionite (black). No major changes are observed between the two spectra indicating reducing equivalency between the agents.

CHAPTER IV

DERIVATION OF DISTANCE RESTRAINTS FOR STRUCTURAL CHARACTERIZATION OF THE PDX-CYP101 COMPLEX

The magnitude of paramagnetic influence is dependent on multiple properties of the paramagnetic compound such as, the number of unpaired electrons, the electron spin correlation time τe, the rotational correlation time, and the magnetic moment (57). Therefore, distance calculations have to be tailored to the parameters of a specific paramagnetic center. To determine the actual broadening range for different paramagnetic metals, and decide which would be most useful for the Pdx-CYP101 complex investigation, broadening effects were calibrated using the reduced ^{15}N-^{1}H HSQC spectra of Pdx^{r}-EDTA coordinated with Gd^{3+} and Mn^{2+}. This exercise confirmed that Gd^{3+} had the largest sphere of influence, with resonances <20 Å broadening beyond detection. Broadening due to Mn^{2+} coordination was distributed across a similar set of peaks but with a smaller magnitude (data not shown). Since a multitude of new resonances appear in the diamagnetic Fe [II] heme-$CYP101^{r}$ spectrum, and more than double the amount of resonance assignments are available, it was inferred that the larger influence of Gd^{3+} would be best suited for the measurement of most restraints.

4.1 Calculation of Distance Restraints from Paramagnetic Relaxation Enhancement (PRE)

Distances from the NMR nucleus to the paramagnetic center were derived using a method developed by Battiste and Wagner (58). Because the total peak volume remains constant after paramagnetic relaxation enhancement (PRE), changes in peak heights (intensities) can be used to measure line broadening indirectly from the observed PREs. A ratio of peak intensities was taken to calculate paramagnetic contribution ($R2^{sp}$), to the observed relaxation rate, R2 through Eq. (5):

$$\frac{I_{para}}{I_{dia}} = \frac{\mathrm{R2}\exp(-\mathrm{R2}^{sp}t)}{\mathrm{R2}+\mathrm{R2}^{sp}} \quad (5)$$

Where I_{para} and I_{dia} are measured intensities of ^{15}N-^{1}H HSQC-TROSY peaks with and without the presence of a paramagnetic center respectively, *t* is the total polarization transfer time (~9 ms) and R2 is the intrinsic diamagnetic transverse relaxation rate for each amide estimated from the peak width of reduced diamagnetic spectra (59). R2 was estimated for each assigned peak from the linewidth (Hz) at half height ($\Delta\upsilon_{1/2}$) in the diamagnetic spectra using $R2=\pi\Delta\upsilon_{1/2.}$ Subsequently, $R2^{sp}$ values were converted into distances using Eq (6):

$$r = \left[\frac{K}{\mathrm{R2^{sp}}}\left(4\tau_c + \frac{3\tau_c}{1+\omega_h^2\tau_c^2}\right)\right]^{\frac{1}{6}} \quad (6)$$

Where *r* is the distance between the electron of the spin label and nuclear spins, τ_c is the estimated global correlation time (~20 ns) of the protein complex from the Stokes Einstein equation, ω_h is the Larmor frequency of proton nuclear spin and *K* is the constant 8.61x10^{-32} cm^{6}s^{-2} (59).

^{15}N-^{1}H HSQC-TROSY spectra of CYP101 and Pdx-EDTA tag chelated to Gd^{+3} in complex with the unlabeled partner were acquired for both oxidation states, and experiments were run in tandem with control samples that lackedGd^{3+}. Intensities were measured for assigned residues, and ratios of the paramagnetic (metal) and diamagnetic (no metal) samples (Fig.4.3) were converted into paramagnetic rate enhancements ($R2^{sp}$) through a linear fit of Eq. (5). Distance restraints were derived through a linear fit of Eq (6). The relationship between intensity ratio and distance (Å) then gives a meaningful range of distance measurements between 21-34 Å (Fig. 4.1). For residues that disappear completely, an upper bound of 20 Å was used in the docking process. Distances from the spin label to various backbone amides in Pdx within the paramagnetic sphere of influence of Gd^{+3} were calculated (Appendix Table 1.)

based on the observed PREs and found to be in good agreement with distances calculated for the very same residues from the crystal structure of Pdx (Fig.4.2). This excellent correlation allowed us to move forward with calculating the Pdx-CYP101 complex distance restraints using a similar methodology.

For structure determination of the complex, it was assumed that the complex is in fast exchange on the NMR time scale since only one set of CYP101 resonances was observed in the spectrum. As explained in chapter 3, it was calculated that approximately 70% of the reduced protein concentration is bound to its partner at any moment assuming a 1:1 ratio in the sample, and a 1:1 binding stoichiometry. Therefore, the observed PRE, $R2^{obs}$, represents only a fraction (F) of the actual PRE, $R2^{sp}$, such that $R2^{obs} = FR2^{sp}$, with F=0.7 and F=0.6 for reduced and oxidized complex respectively. It was necessary to correct the experimentally determined PREs by 1/F before using $R2^{sp}$ in the distance calculations.

4.2 Analysis of PRE-derived Distance Restraints

The ^{15}N-^{1}H HSQC-TROSY of $CYP101^{o}$ and $CYP101^{r}$ in complex with Pdx^{o} and Pdx^{r} yielded 39 and 95 peaks respectively, which met the 0.85 ratio threshold for further consideration to be used as distance restraints in the docking simulations (Fig. 4.3). The 0.85 threshold was used for two reasons. First, as demonstrated by the curve in Fig. 4.1, small changes in ratios measured to be >0.85 lead to large differences in the distance calculation. Therefore, assuming some degree of experimental error, ratios >0.85 offer the least accurate measurements. Secondly, previous groups report the best agreement with known three-dimensional structures using the 0.85 cutoff (58). The fewer number of significantly broadened peaks in the oxidized complex was a function of the fewer visible resonances and available assignments in the paramagnetic state Fe [III] state. Peaks within 8 Å of the heme broadened beyond detection and additional spectral overlap in $CYP101^{o}$ complicates the assignment process.

Overall however, broadening patterns between the oxidized and reduced complex spectra were remarkably similar suggesting that the binding site for the two redox states is the same (Fig.4.5). As expected, there is strong evidence for 1:1 binding stoichiometry, and the peaks observed to broaden drastically, agree well with those residues known to be within or near the Pdx binding site on the proximal face of CYP101 (Fig. 4.4). Interestingly, one region of CYP101 did consistently show differential broadening profiles between the oxidized and reduced complexes. The SRS-1 region surrounding and including B' Helix between residues 84-96 was significantly less broadened for every available resonance in the reduced complex, resulting in longer distances for these resonances (Table 4.1 and 4.2). This region is known to be dynamically involved in substrate gating, and these differences could have profound implications for the redox-dependent Pdx effector mechanism.

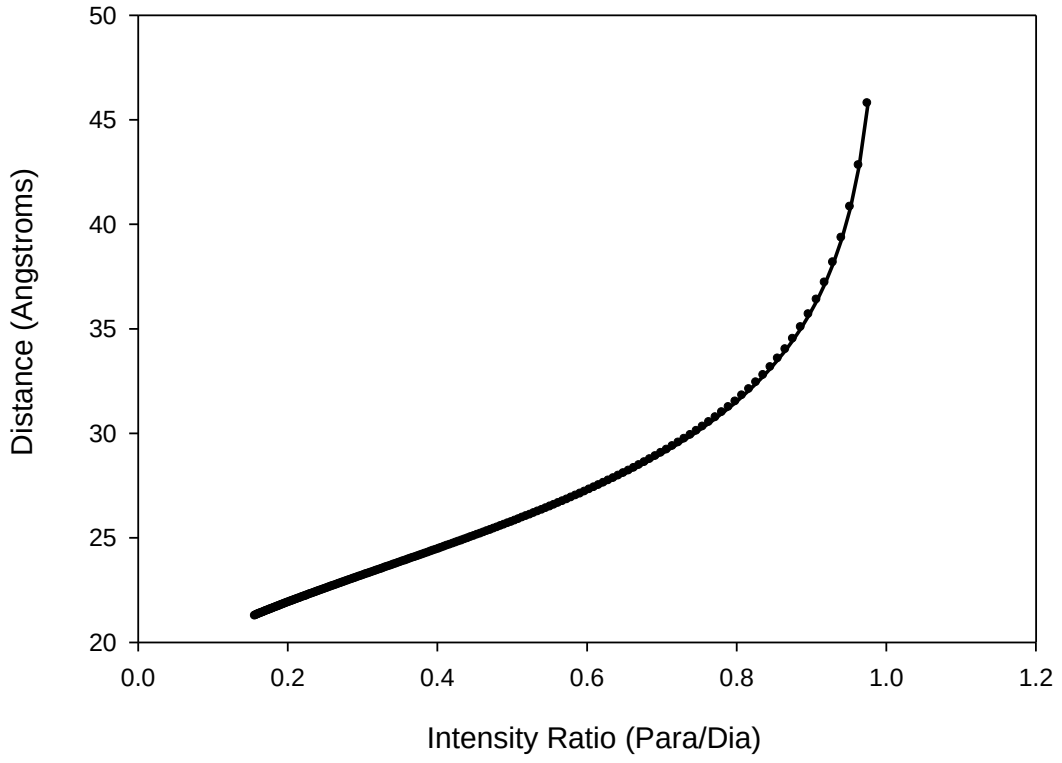

Figure 4.1. **Correlation Plot for converting Intensity Ratios to Distances.** Varying intensity ratios of (I_{para}/I_{dia}) were converted into distances using the theoretical equations (5) and (6) in the text.

Table 4.1 Distance restraints calculated for CYP101^{r} from experimentally measured PREs

Residue no.	Measured (Å)[a]
38	28.5
77	20.0
78	20.0
84	26.2
85	26.4
91	27.9
92	29.9
93	27.5
99	24.9
119	27.2
120	27.2
208	31.5
226	29.2
227	25.1
230	20.0
233	27.2
234	27.0
235	27.3
236	28.3
247	27.2
296	29.0
298	26.2
300	26.4
305	28.8
306	24.1
307	26.9
309	27.1
310	25.2
312	25.4
314	26.7
331	32.2
345	30.8
347	27
351	29.3
359	24.2

[a]Distances are measured from the intensity ratios calculated for the HN backbone amide resonances of ^{15}N labeled CYP101^{r} in complex with spin labeled Pdx^{r}-EDTA- Gd^{3+}. All distance measurements were docked with bounds of ± 4 Å.

Table 4.2 Distance restraints calculated for CYP101^{o} from experimentally measured PREs

Residue no.	Measured (Å)[a]
54	30.4
67	30.5
68	26.8
70	25.1
80	20.0
82	20.0
84	25.5
85	22.4
92	28.3
93	26.6
94	26.8
96	27.0
101	20.0
123	26.4
167	30.5
217	30.4
230	20.0
243	27.1
245	31.0
305	25.0
306	23.6
307	26.8
308	28.1
309	24.1
312	27.0
326	29.2
330	29.4
348	26.6

[a]Distances are measured from the intensity ratios calculated for the HN backbone amide resonances of ^{15}N labeled CYP101^{o} in complex with spin labeled Pdx^{o}-EDTA- Gd^{3+}. All distance measurements were docked with bounds of ± 4 Å.

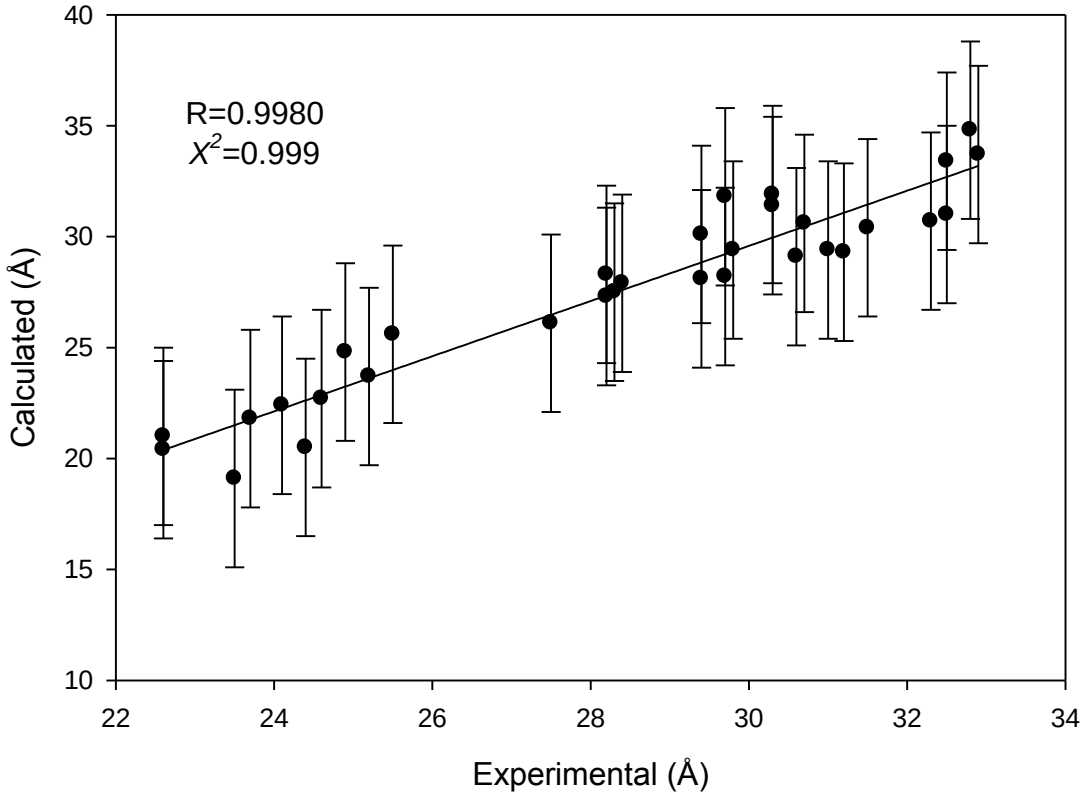

Figure 4.2.**Correlation between back calculated and PRE measured distances.** Plot of the correlation between back-calculated distances from the reduced Pdx crystal structure and distances calculated from experimental PRE measurements in the reduced Pdx-CYP101 complex. Experimental distances were calculated by applying the theoretical conversion equations (5) and (6) in the text to the PRE intensity ratios measured using Pdx^{r} –EDTAsl-Gd^{3+}. The correlation coefficient was ~99% for residues between 20-34 Å from the paramagnetic center. Error bounds of ± 4Å were applied to every measurement.

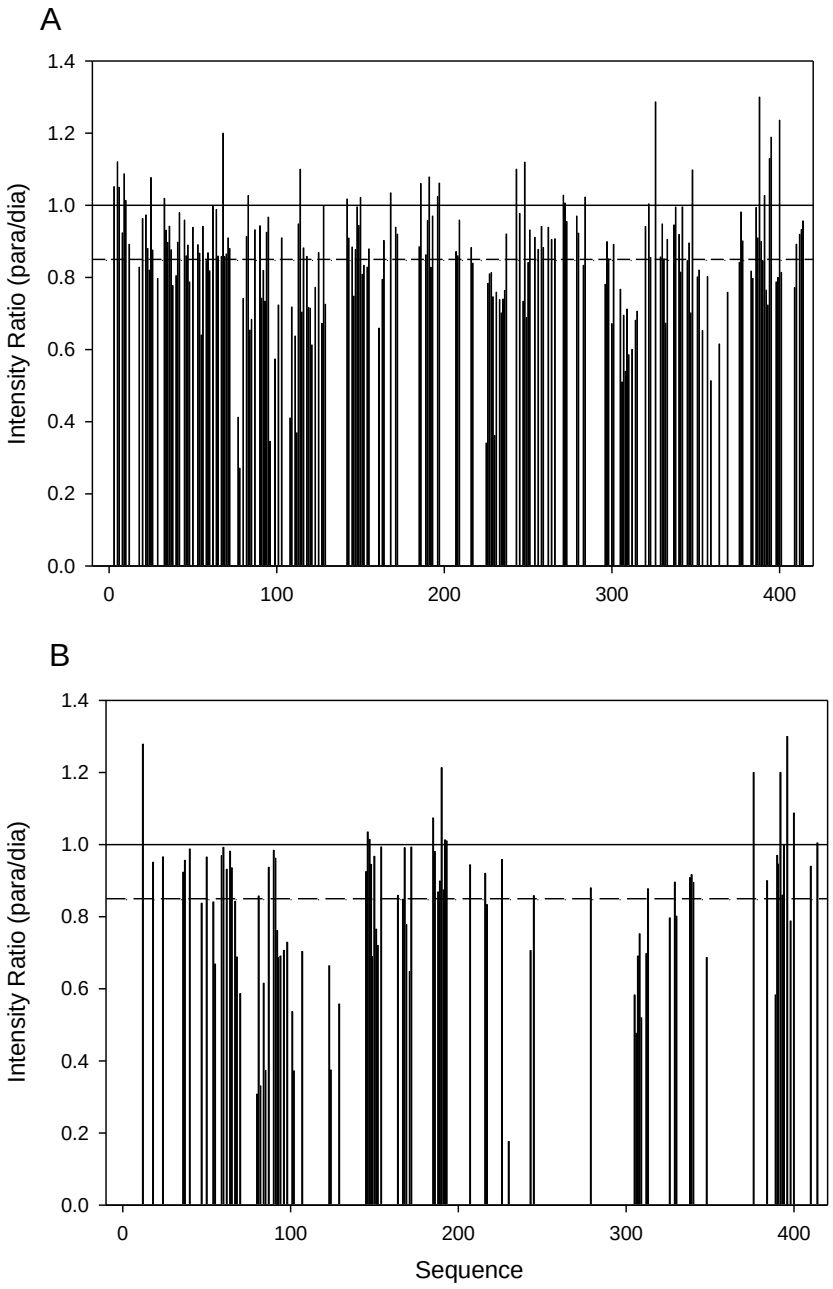

Figure 4.3.**PRE Intensity Ratios measured for Reduced and Oxidized CYP101.** Intensity Ratios of various ^{15}N-^{1}H resonances in the CYP101 TROSY spectra are plotted versus residue number for the reduced (A) and oxidized (B) Pdx-Cyp101 complexes. A value of 0.85 was used as the maximum threshold for inclusion in our distance calculations and is shown by dashed lines. Absence of bars indicates no assignments were available at the sequence position or spectral overlap prevented accurate quantification.

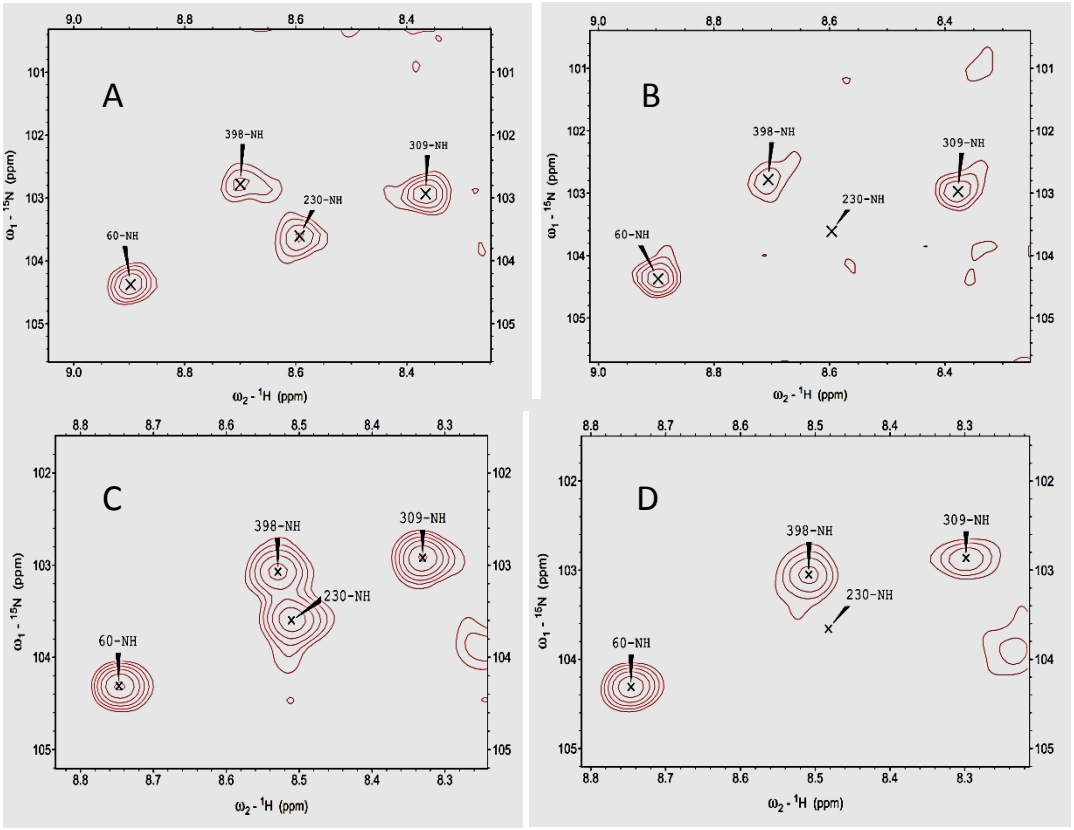

Figure 4.4. **Paramagnetic Broadening between the oxidized and reduced complexes.** Regions of ^{15}N-HSQC-TROSY spectra of CYP101^{r} (A,B) and CYP101^{o} (C,D) bound to Pdx^{r} – EDTA and Pdx^{o}-EDTA respectively, without (A,C,E,G) and with (B,D,F,H) Gd^{3+} coordinated. Specific residue numbers are indicated with labels. Residue 230 on the proximal face of CYP101 is shown broadening beyond detection in both the reduced (A,B) and oxidized (C,D) spectra. Both oxidized and reduced complex spectra were processed similarly and the contour levels are the same between them.

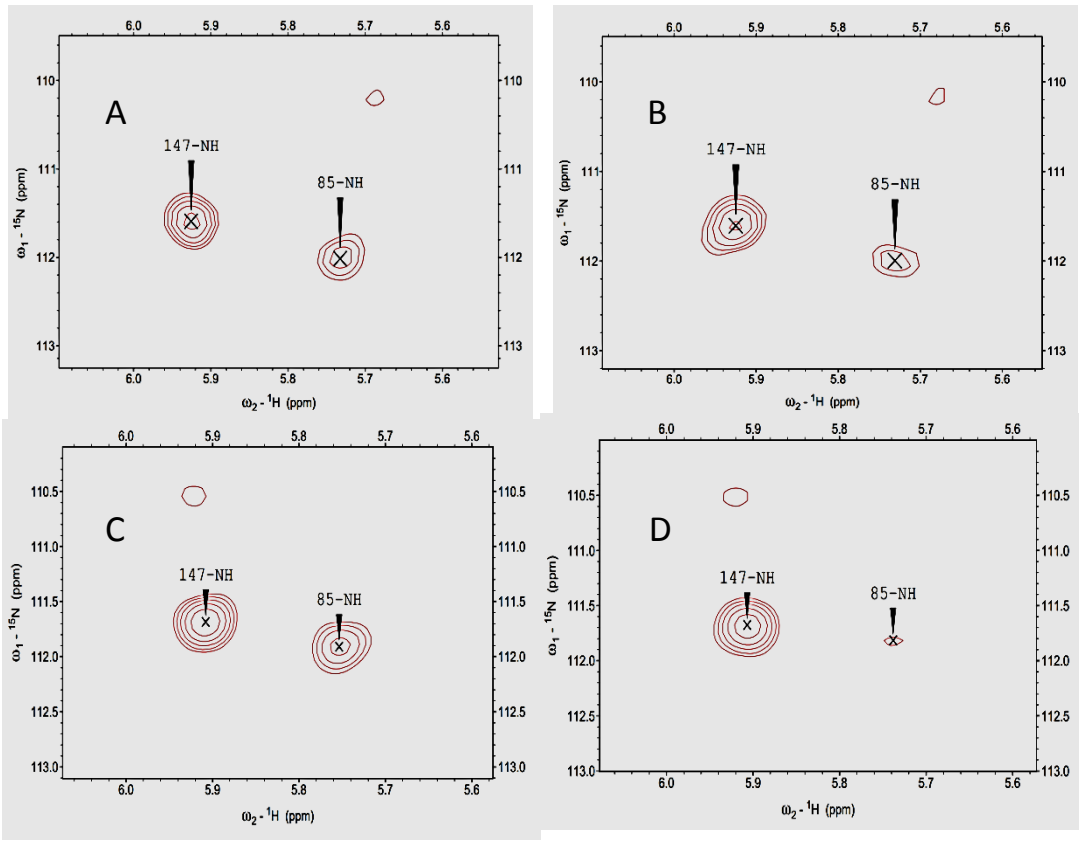

Figure 4.5 .**Differential Paramagnetic Broadening between the oxidized and reduced complexes.** Regions of ^{15}N-HSQC-TROSY spectra of CYP101^{r} (A,B) and CYP101^{o} (C,D) bound to Pdx^{r} –EDTA and Pdx^{o}-EDTA respectively, without (A,C) and with (B,D) Gd^{3+} coordinated. Specific residue numbers are indicated with labels. Residue 85 at the B-C Loop exhibits differential broadening between the reduced (E,F) and oxidized (G,H) spectra. Both oxidized and reduced complex spectra were processed similarly and the contour levels are the same between them.

Several peaks outside of the immediate vicinity of the binding site demonstrated significant broadening, and therefore, it was necessary to delineate ambiguous PRE contributions arising from non-specific binding, free metal, flexibility of the EDTA spin label, and the conformational search for the binding site. To calibrate non-specific broadening from metal, free metals were added to solution as controls in separate experiments with each ^{15}N-labeled protein without the EDTA spin label conjugation. Using these control experiments, non-specific PRE effects from just the free metal in solution were delineated from specific metal effects (data not shown). Localized broadening at sites distant from the primary interaction site that could complete the coordination sphere for Gd^{3+} without coordinating to the EDTA tag were identified during these experiments and supposed to arise from non-specific metal binding residues on the surface of CYP101 (e.g. Glu152-Glu156). Calibration of the non-specific PRE effects in this manner allowed us to quickly determine if non-EDTA coordinated excess metal was free in solution during our complex experiments, helped identify non-specific binding sites, and reduced the possibility of mistakenly including these contributions in the distance calculations.

One alternate possibility of interpreting some of the PRE effects that are far away from the primary interaction site of Pdx and CYP101 is that there may be more than one binding site for the two proteins. However, the Pdx-P450cam complex is known to be a highly specific interaction. The site-specific ^{15}N-^{1}H HSQC broadening profiles on CYP101 and Pdx observed here due to binding of the partners, is consistent with other groups also reporting site-specific spectroscopic changes for the Pdx-CYP101 complex (60). Moreover, while the specific interaction is retained in presence of different metals and other spin labels (e.g. MTSL), the non-specific contributions differ considerably between them. Hence non-specific PREs are likely contributions from the conformational search process, spurious binding sites and excess metals; not from multiple protein binding sites.

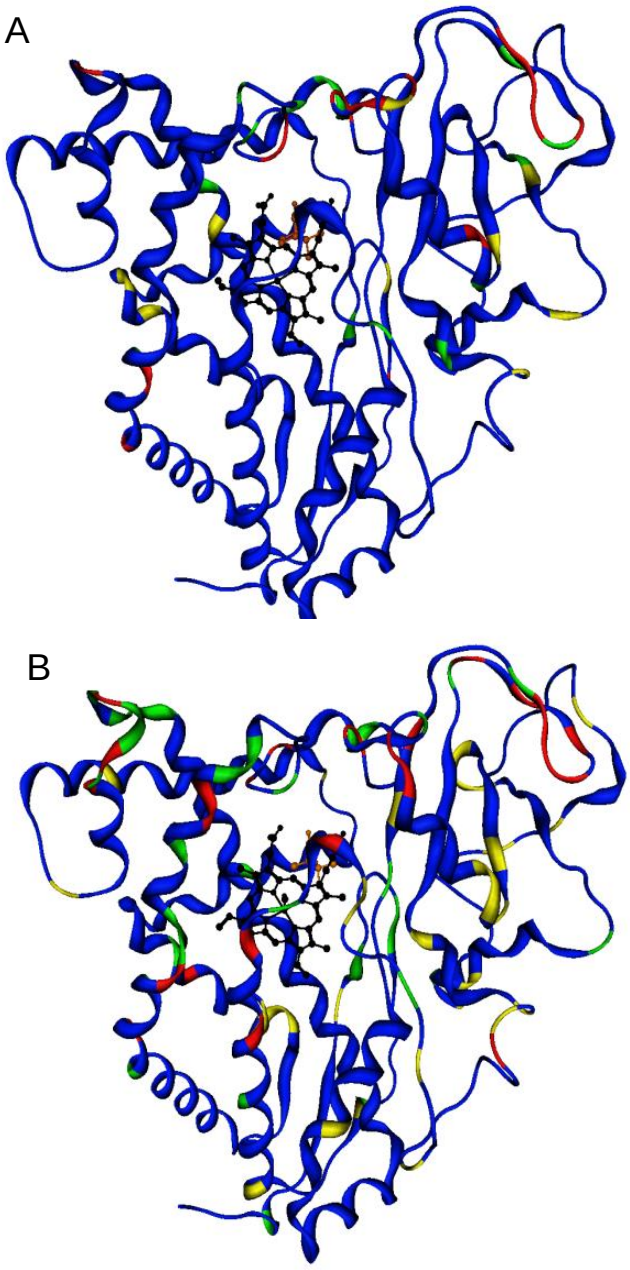

Figure 4.6.**Comparison of PRE Broadening Patterns in oxidized versus reduced complex.** Spectral broadening of CYP101 NH resonances mapped on the structure of CYP101 as a result of PREs from the spin label on Pdx in A) oxidized and B) reduced Pdx-CYP101 complex. Previously determined individual crystal structures of oxidized and reduced Cyp101 (PDB ID: 2CPP and 3CPP) are used to depict the paramagnetic broadening patterns. Red residues correspond to resonances with extreme broadening (ratios < 0.6). Green residues correspond to resonances with moderate broadening (ratios > 0.6 and < 0.8). Yellow residues correspond to resonances with slight broadening (ratios > 0.8). Blue residues are either unassigned or have no significant broadening (ratios > 0.85).

Another factor to consider in distance calculations is the influence of motion on PREs, which can be considerable depending on the confinement of the paramagnetic center. Rigid paramagnetic centers with respect to the protein under investigation are optimal, as they give the most accurate distance calculation from a singular, well-defined location. In this study, the EDTA spin label was relatively long, raising concerns about its flexibility. To reveal whether the label was sampling isotropic motions relative to the protein, pseudo-contact shift (PCS) experiments were performed. If the paramagnetic center is sampling isotropically the anisotropic $\Delta\chi$ tensor component of PCS will average to zero, and hence the chemical shift effect averages to zero. Coordinating a metal with fast relaxing electrons, such as Tb^{3+}, in place of Gd^{3+}, resulted in small but distinguishable contact shifts in the ^{15}N HSQC spectra of Pdx and CYP101 (Fig 4.6).This indicates sufficient label rigidity and metal confinement for accurate PRE measurements.

PRE distance restraints provide information in only one dimension of a three-dimensional coordinate frame and therefore, additional restraints are critical for precise structure refinement. PCS on its can be very useful in collecting both distance and orientational information, and indeed certain groups reported using this same EDTA based metal chelating tag for quantitative PCS experimentation (53, 61, 62). However, in our experiments Tb^{3+} coordination resulted in peak doublets of similar intensity (Fig.4.6). Other groups reported the same doubling result with this label, and attribute the effect to the possibility of two stereoisomers of the EDTA-metal complex (52, 63). Consequently, this EDTA spin label gave data that was too difficult to interpret for quantitative PCS measurements, and consequently Tb^{3+} was only used to establish a necessary level of confidence in the rigidity of our spin label.

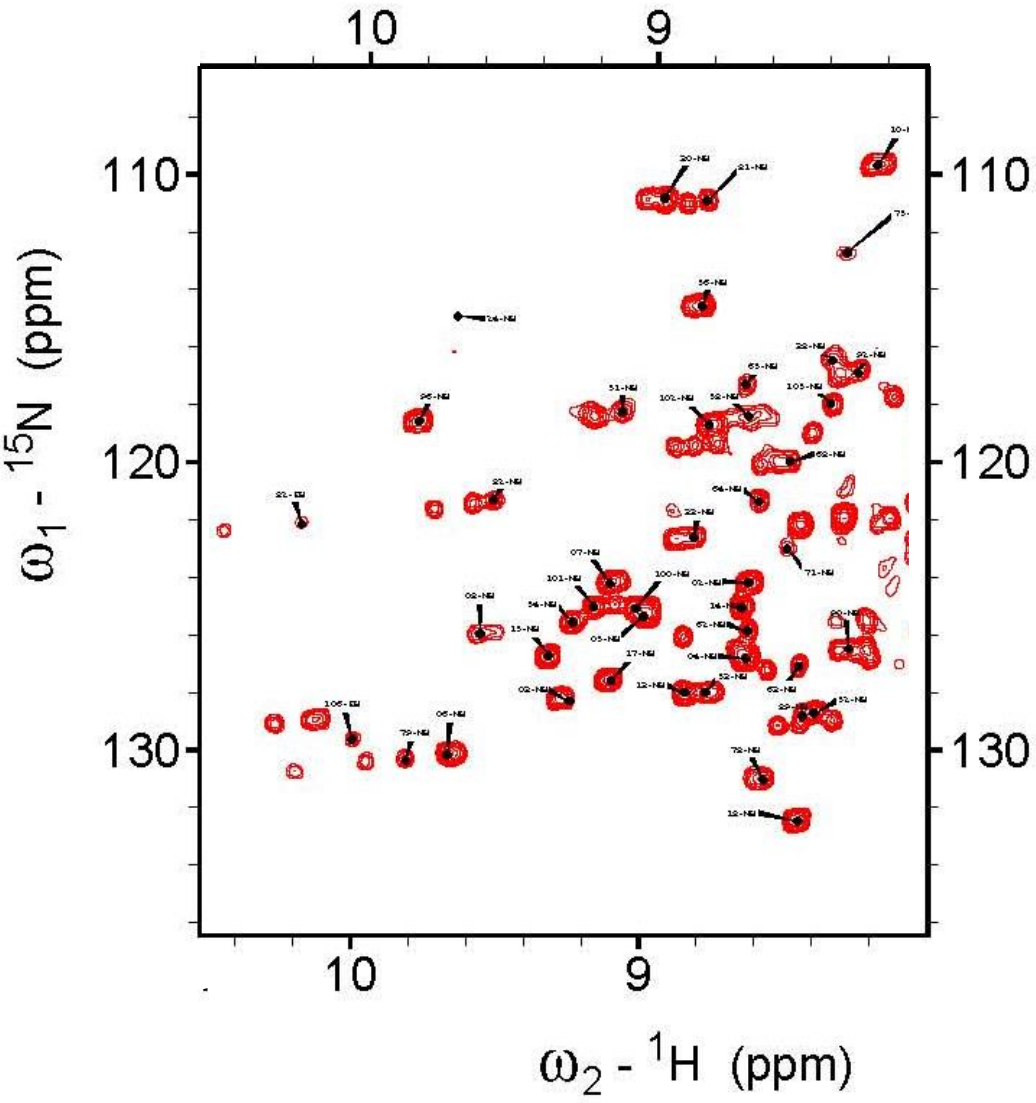

Figure 4.7. **Spectral Changes induced in Pdx by Pseudo-contact shifts from a Tb^{3+}-coordinated spin label.** Region of ^{15}N-^{1}H HSQC spectra of oxidized Pdx-EDTA-Tb^{3+} demonstrating the pseudo-contact shifts and peak doubling which occurred as a result of 2 stereoisomers being present during metal coordination.

CHAPTER V
COMPLEX STRUCTURE CALCULATION AND ANALYSIS

5.1 Docking of Pdx with CYP101

To determine the structures of oxidized and reduced Pdx-CYP101 complexes, the two proteins were docked using the Molecular Operating Environment (MOE) software (Chemical Computing Group). Starting coordinates for the individual proteins were obtained from the Protein Data Bank, with PDB identifiers 2LQD, 1XLN, 3CPP, and 2CPP for Pdx^r, Pdx^o, $CYP101^r$, and $CYP101^o$ respectively. The S-cysteaminyl-EDTA metal chelating spin label was built in MOE and bonded to Cys73. To model the most likely position of the EDTA spin label, Pdx-EDTA was energy minimized using the AMBER99 force field parameters designed for proteins. Despite the label having some degree of flexibility, the energy minimized position was considered as the average position, and was therefore held constant through the remainder of the docking simulation (Fig. 5.1). A total of 67 and 62 PRE distance restraints are available for the reduced and oxidized complexes respectively. These restraints can be categorized into two sets – the first set comprised restraints that were calculated from PRE measurements carried out on ^{15}N labeled Pdx in complex with unlabeled CYP101, while the second set comprised restraints calculated from PRE measurements on ^{15}N CYP101 in complex with unlabeled Pdx. In each case, Pdx was tagged with the EDTA chelator bound to Gd^{3+}. For the complex structure calculation, only the second set of restraints was used which corresponded to 35 for reduced complex and 28 for the oxidized complex (Table 4.1 and 4.2). Compared to the seven restraints used in determining the initial oxidized complex structure (17), this represents a considerable improvement in the number of restraints. In addition, a maximum distance of 20 Å between the Fe_2S_2 cluster and the heme was set as a restraint in both complexes.

During the docking process, initial positioning of Pdx was achieved by weighting the distance restraints. First priority was given to the distances

between the [2Fe-2S] and the heme prosthetic groups, as well as residues whose resonances broadened out beyond detection. Both of these distance restraints were set a maximum of 19.99 Å and were never violated. Each has precedent in the literature with <20 Å being the distance between metal cofactors for physiologically relevant electron transfer rates, and the distance between NMR nuclei and $Gd^{3+}$for complete resonance broadening (34, 43, 52, 64). Second priority was given to residues that had an intensity ratio (I_{para}/I_{dia}) between 0.5-0.75. These residues were measured to be no more than 28.5 Å from the paramagnetic center. Peaks <0.75 were considered not to arise from non-specific broadening effects and a strong reflection of the final docked structure. Last priority was given to those residues demonstrating intensity ratios >0.75. To minimize the contribution of false positives, residues in close proximity that shared similar broadening ratios were weighted more heavily across all tiers. For all residues within the second and third tiers error windows of ±4 Å were applied. For PRE measurements, this error window has been shown to result in the most robust structure calculations (17, 58, 65). Docking was continued through manual sampling of the conformational space until the best fit between measured and calculated restraints was achieved. Removing the label and then energy minimizing the interfacial residues gave the final complex structure used in analysis (Fig. 5.2 and 5.3). In the final complex structures all residues fell within ± 4 Å, except for residues 84, 85, 300, 305, and 314 in the reduced complex and residues 123 and 217 in the oxidized complex. The large amount of variability witnessed in the 300-314 loop region is thought to be due primarily to its considerable flexibility.

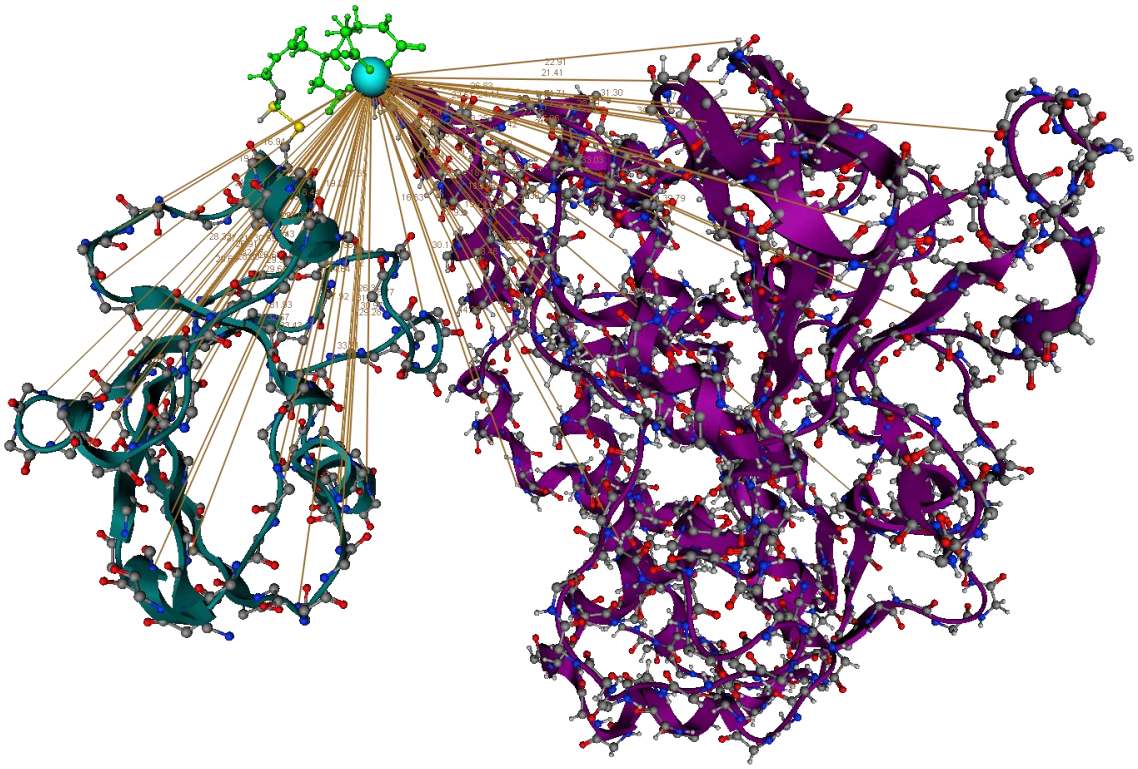

Figure 5.1.**Pdx-CYP101 Complex modeled with the EDTA metal chelating spin label.** Cartoon representation of the Pdx-Cyp101 complex modeled with the EDTA metal chelating label. Pdx (teal) is shown conjugated to the EDTA spin label (green) with Gd^{3+} coordinated (cyan). Gold lines are drawn between Gd^{3+} and amide bonds on the on the Pdx and CYP101 (magneta) backbone for residues within the 34 Å broadening range.

5.2 Structural Analysis of the Oxidized and Reduced Pdx-CYP101 complexes

Disregarding the inherent structural differences that existed in the initial starting structures of oxidized and reduced Pdx as also oxidized and reduced Cyp101, the final complex structures calculated for both oxidation states are quite similar within experimental error (Fig. 5.3 and 5.4). Pdx binds to CYP101 at a similar site in both complexes. Also, the binding interface in both complexes is similar as well. Three key interactions predicted by previous structural and mutagenesis studies formed part of the binding interface in our structures (Fig. 5.4) (34, 66, 67). Two salt bridges, Asp38 (Pdx)-Arg112 (CYP101) and Arg66 (Pdx)-Glu76 (CYP101), that are critical for affinity and electron transfer in the Pdx-CYP101 complex were observed within the proper distance range to support their electrostatic interaction (Fig. 5.5). Additionally, Trp106, the C- terminal residue of Pdx shown repeatedly from kinetic and mutagenesis studies to be a key modulator of binding and electron transfer was situated next to the hydrophobic pocket containing Ala113 on CYP101. It is not clear at this stage how Trp106 exerts its influence on this hydrophobic pocket, allowing it to modulate the affinity and electron transfer. Further structural analysis is needed to discern its role.

An interesting observation made from the PRE data comparison of the oxidized and reduced complexes was that the SRS-1 region, which includes the the B'-Helix, shows differential broadening profile between the oxidized and reduced complexes. The distance of the B'-Helix in the SRS-1 region in the oxidized complex from the Pdx binding site was consistently measured to be shorter than that in the reduced complex, indicating that this region is closer to Pdx, implying that it may be sampling an effectively more open conformation in the oxidized complex relative to the reduced complex. Unfortunately, distance measurements to the F-G loop (which is also part of the SRS-1 region) could not be made, since it is not within the 34 Å paramagnetic radius of Gd^{3+}, and consequently no PRE data was available for this region. Since the docking

method used here is not precise enough to pry out minute structural differences between the complexes, the exact nature of these differences at the B'-Helix cannot be discerned at this point. However, given the importance of this region in substrate binding, it's likely that these differences have implications for Pdx effector activity. It is possible that redox-dependent Pdx binding modulates dynamics of this region; favoring change from sampling of an open conformational subset in the oxidized complex to a closed conformational subset in the reduced complex. This is in line with the Pochapsky model which hypothesizes that effector activity promotes a closed subset of catalytically competent conformations that prevent substrate loss prior to O_2 uncoupling.

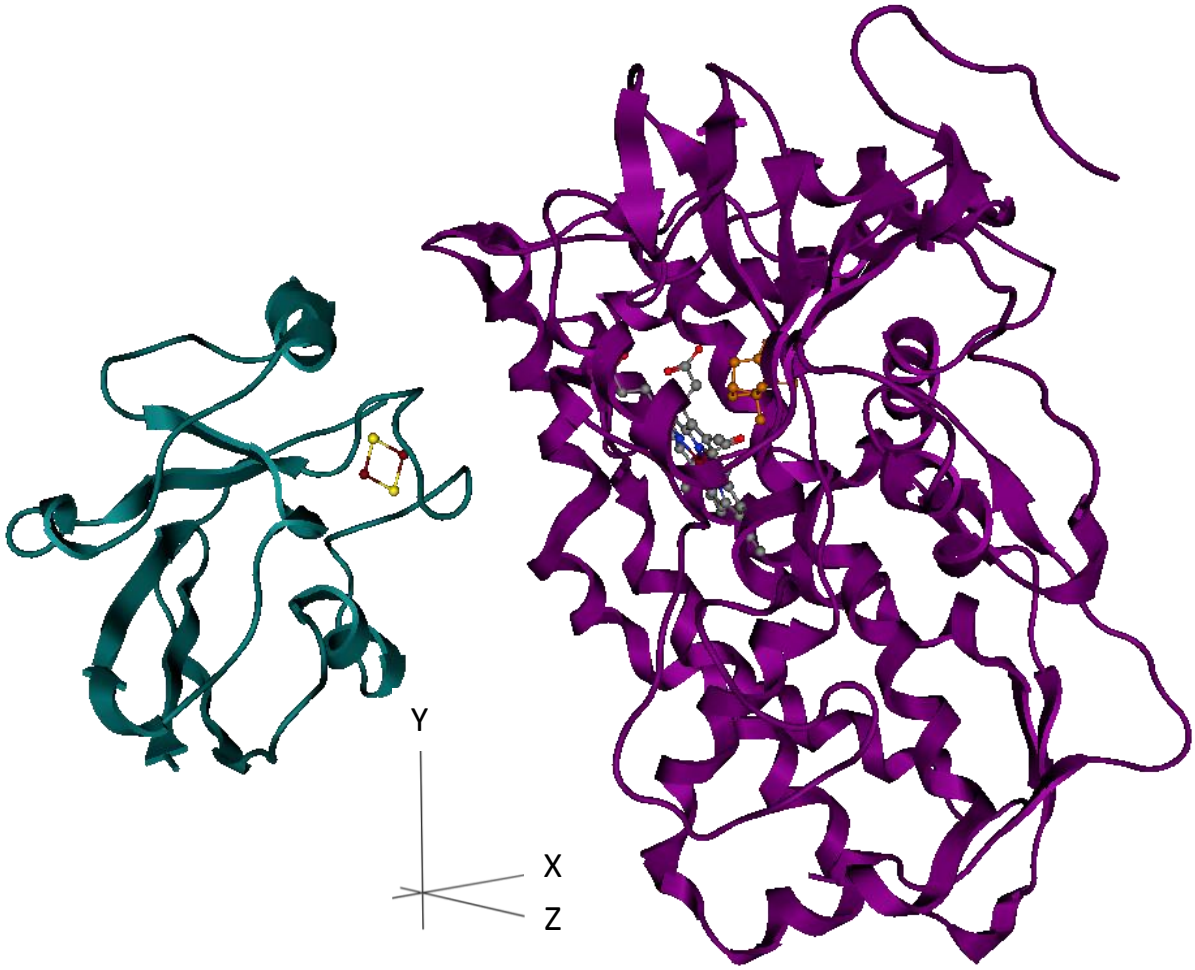

Figure 5.2.**Solution NMR structure of the Pdx^{r}-CYP101^{r} complex**. Cartoon representation of the solution NMR Structure of Pdx^{r} (teal)-CYP101^{r} (magneta) derived from PRE restraints, docking, and energy minimization in MOE. The [2Fe-2S] metal cluster (yellow and red) is shown docked at the proximal face of the heme (gray) with camphor (orange) bound in the active site.

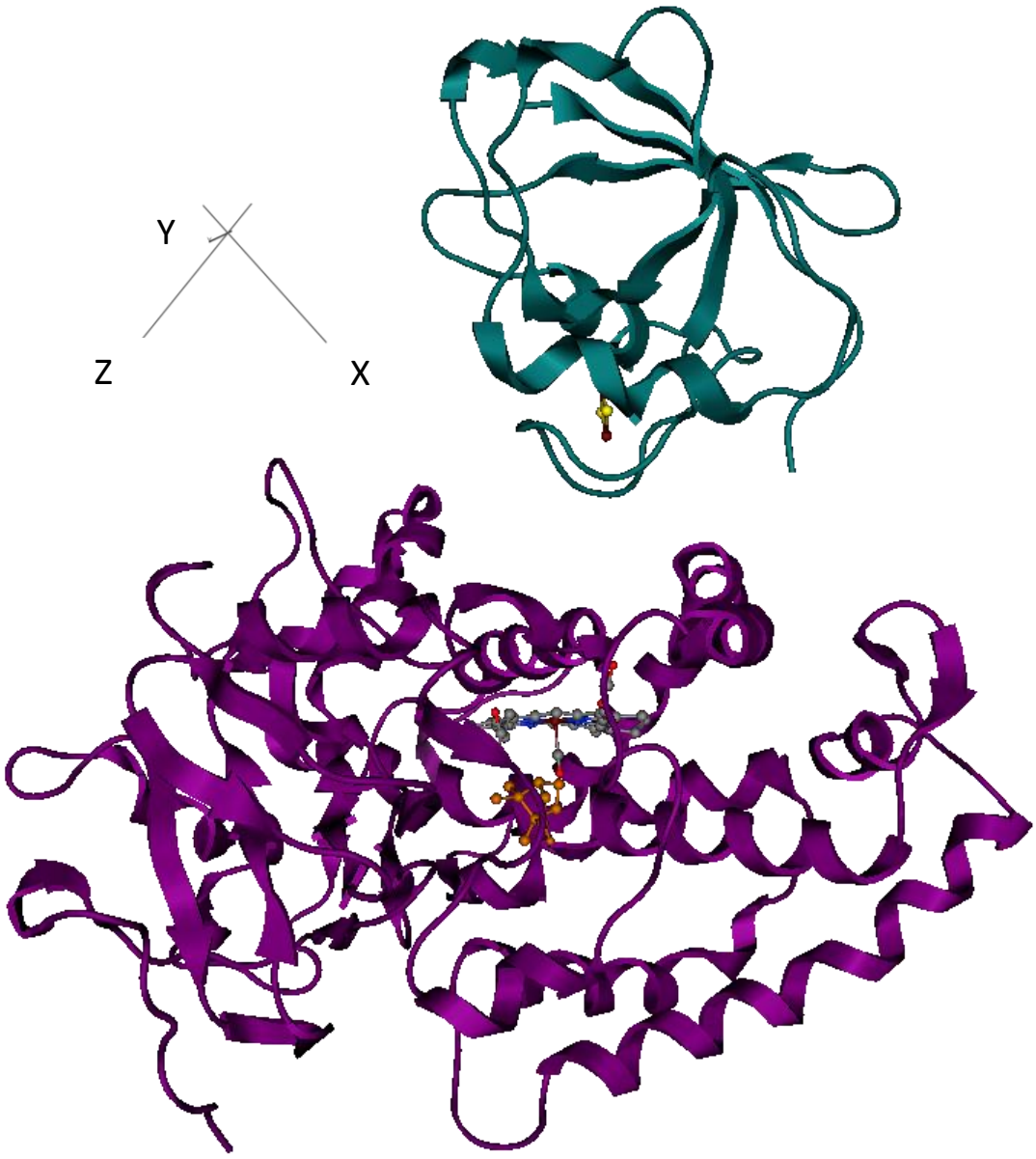

Figure 5.3.**Solution NMR structure of the Pdx^{r}-CYP101^{r} complex (alternate view).** Cartoon representation of the solution NMR Structure of Pdx^{r} (teal)-CYP101^{r} (magneta) derived from PRE restraints, docking, and energy minimization in MOE. The [2Fe-2S] metal cluster (yellow and red) is shown docked at the proximal face of the heme (gray) with camphor (orange) bound in the active site.

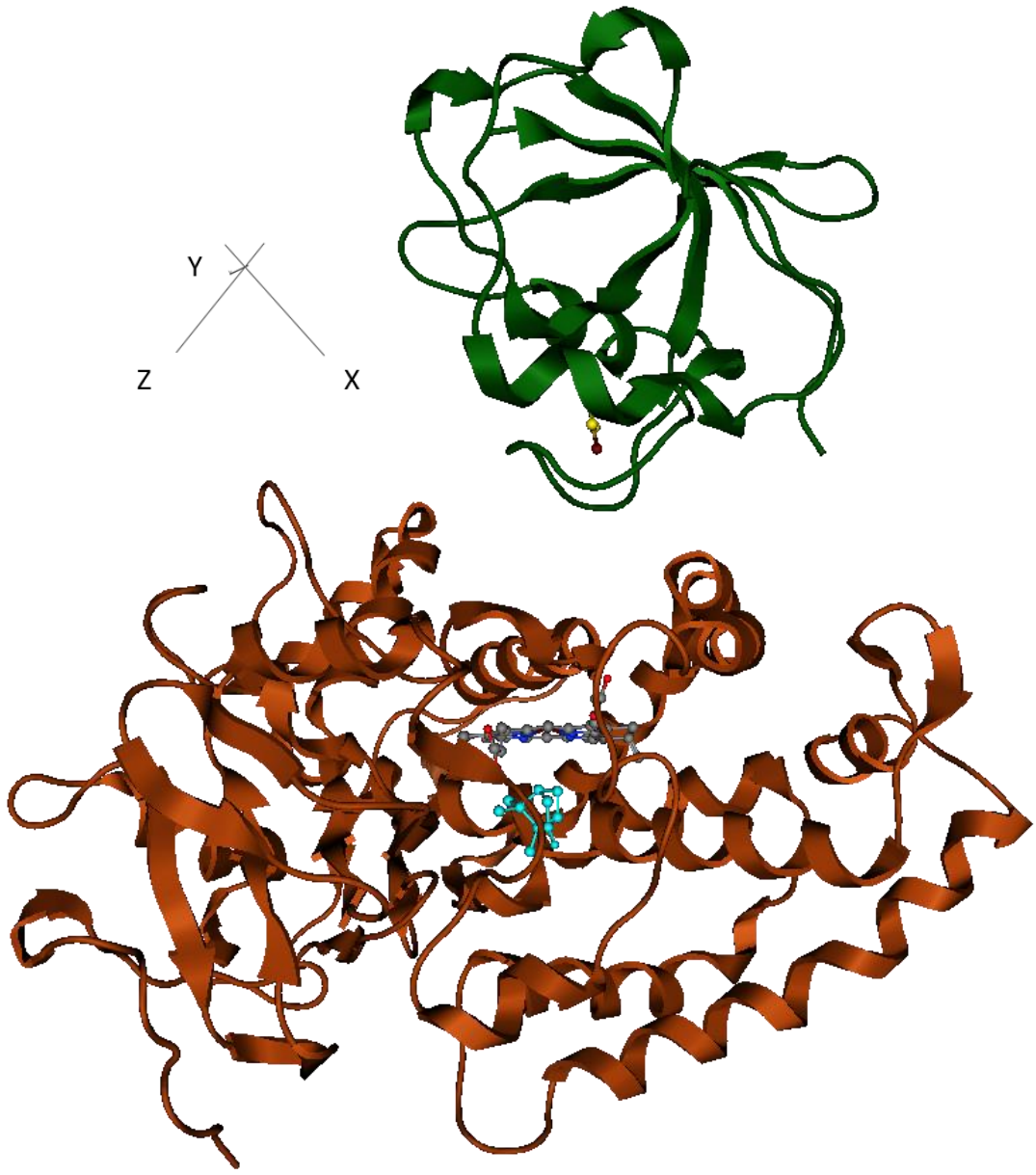

Figure 5.4. **Solution NMR structure of the Pdx^{o}-CYP101^{o} complex.** Cartoon representation of the solution NMR Structure of Pdx^{o} (green)-CYP101^{o} (copper) derived from PRE restraints, docking, and energy minimization in MOE. The [2Fe-2S] metal cluster (yellow and red) is shown docked at the proximal face of the heme (gray) with camphor (cyan) bound in the active site.

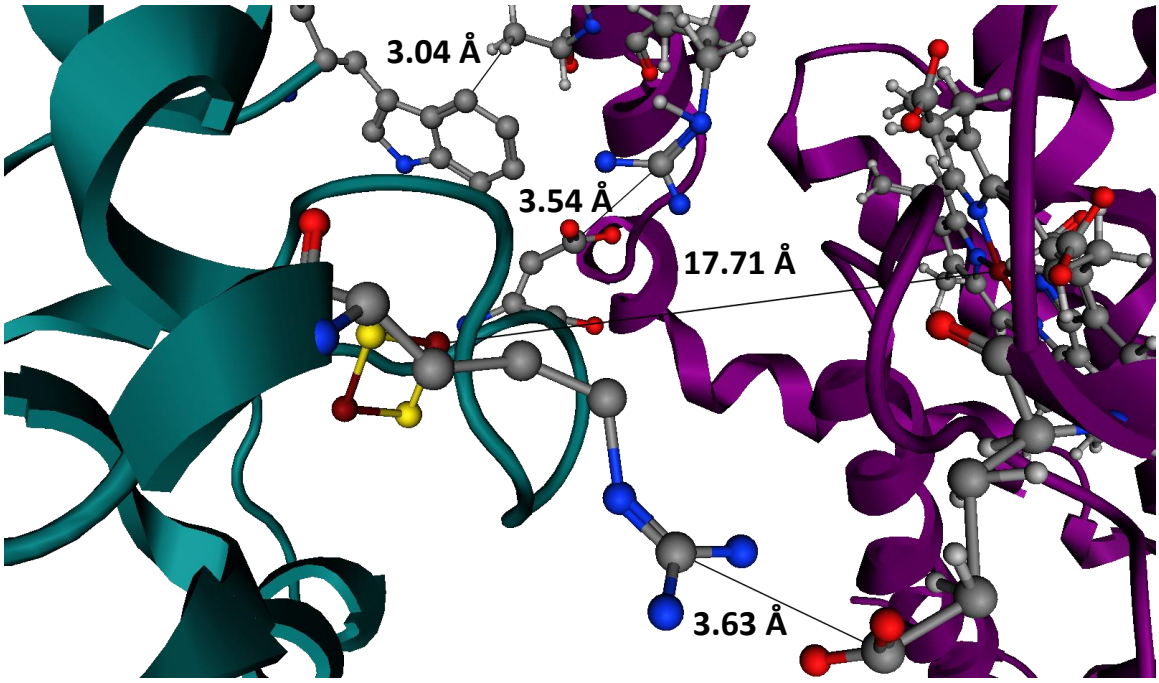

Figure 5.5.**Key interactions in the reduced Pdx-CYP101 Complex**. Three key interactions at the Pdx^{r}-$CYP101^{r}$ interface are observed in the solution NMR structure. Distances are labeled between the sidechains of interacting residues and the iron atoms of the metal centers. From top to bottom: Trp106 on Pdx in hydrophobic contact with Ala 113 on CYP101, Asp38 on Pdx forms a salt bridge with Arg112 on CYP101, and Arg66 on Pdx forms a salt bridge with Glu76 on CYP101.

5.3 Comparison with Other Structural Studies

While this manuscript was under preparation, the Poulos group using X-ray crystallography also solved the structure of the chemically cross-linked oxidized and reduced Pdx-CYP101 complex (37). The solution NMR structure determined here is in good agreement with the Pdx binding site found in those co-crystal structures. Contrary to our findings, the investigators in that study have proposed that Pdx binding promotes CYP101 to favor an open conformation in the substrate access channel that is critical for catalytic activity. The Pdx effector mechanism is therefore linked to a closed to open conformational change that establishes a water-mediated H-bond network required for proton-coupled electron transfer and O_2 activation. These conclusions have to be viewed with some skepticism however, since the reduced co-crystal structure is solved with the product bound instead of the substrate, lending a certain amount of doubt to the validity of the open conformation in the context of the effector mechanism that works prior to and during substrate turnover, but not after. It is possible that the open conformation is accessed to release the product and the crystal structures thus do not provide adequate explanation for how the effector mechanism is redox-dependent. Interestingly, in their study, two co-crystal structures were published for the oxidized complex; one in which the B'-Helix is modeled exactly as in the reduced, and another which fails to model the B'-Helix at all, likely due to the large dynamic amplitude in this region. The structure lacking a modeled B'-Helix is also seen in the absence of substrate, a state known to favor the open conformation (68). A probable explanation for this observation is that crystal packing effects between adjacent molecules may favor crystallization in an open state. The open conformations in CYP101 trapped in these co-crystal structures therefore may not provide an accurate representation of changes occurring in response to Pdx effector modulation and need further investigation in solution.

Nevertheless, the data collected here clarifies several aspects with regards to redox control of the Pdx-CYP101 interaction. Multiple studies have

suggested, based on mutagenesis and computer simulations, that the electron pathway or binding site is different between the two electron transfer steps (34, 67), with a few suggesting that NMR spectral changes observed on the distal face of CYP101 were caused by 1:3 or 1:6 aggregates of CYP101:Pdx. It was further suggested that Pdx^{o} binding to the substrate access channel stabilized an energetically strained conformation of the I-Helix that facilitates faster binding of Pdx^{r} before CYP101 uncoupling occurs. Our data definitively precludes the possibility of aggregates forming in solution as the source of modifications on the distal face of CYP101. If such aggregates are indeed present, broadening patterns on CYP101 would have reflected the relevant stoichiometry and additionally, more residues at or near the substrate access channel would have shown intense broadening. Also, since the PRE measurements for the oxidized and reduced complexes converged on the same position it seems highly unlikely that significantly different binding sites exist and undermines the proposal of different electron transfer pathways. Ultimately, it allows us to set aside the possibility that the Pdx effector mechanism acts through a redox dependent selection of the binding site, and points towards a mechanism involving redox modulated conformational selection on CYP101.

CHAPTER VI
CONCLUSIONS AND FUTURE DIRECTIONS

The nature of the Pdx-CYP101 interaction and its role in Pdx effector activity has mystified researchers in the P450 area for quite some time. The work performed in this thesis is an important first step in answering some fundamental questions on how these two proteins interact in a redox-dependent manner. Conclusive evidence from this study demonstrates that Pdx^o and Pdx^r bind to same site on the proximal face of $CYP101^o$ and $CYP101^r$ respectively, with 1:1 stoichiometry. Since the Pdx binding site and the complex structures are the same between the two redox complexes, redox-dependent effector activity is more likely to be the result of redox-modulated conformational dynamics. Given these findings, it is unlikely that different electron transfer pathways exist between the redox complexes as has been previously speculated.

An important question still remains in how Pdx binding propagates redox-dependent changes to the substrate access channel. Although the recent co-crystal structures argue in favor of an open conformation for both redox states at the F-G loop and I-Helix which activates and orchestrates the catalytic machinery, the role of dynamics in modulating some of these changes cannot be understated. While not definitive, our data supports the conformational dynamics model of Pdx effector activity that postulates the Pdx effector mechanism works through a redox-modulated selection of a closed subset of conformations. This closed conformation is hypothesized to enhance catalysis by preventing substrate release prior to electron transport and product turnover. The farther distances measured at the B'-helix in the reduced complex structure are representative of the closed conformational subset.

The in-solution PRE measurements have an attribute of reporting on the dynamic ensemble of conformations, effectively providing information on the average conformational distribution over the entire length of the experiment. However, by starting with predetermined three-dimensional individual crystal

structures, a severe limitation is placed on the structure calculation by foregoing the dynamic ensemble nature of the complex structure. Small conformational changes upon binding are also quite difficult to model correctly *in silico* with the small number of PRE restraints that were used in docking the two proteins. Deciding whether differences between the measured and calculated distances are a result of experimental error or conformational changes becomes an ambiguous exercise in this case. The minor changes witnessed in the ^{15}N HSQC-TROSY spectra of CYP101 before and after binding of Pdx, indicate no major secondary structure changes take place, and the recent crystal structures corroborate this observation. Therefore, trying to capture the subtle conformational differences and in particular, the dynamic differences, that, in all likelihood, define the Pdx effector mechanism may require a more sensitive method than PRE.

There are some additional ways in which this complex structure model can be improved. One possibility is to include orientational information in the structure calculation, to refine the relative orientation of the two proteins, which currently is only a rough approximation. Orientational restraints in the form of residual dipolar couplings (RDC) can be experimentally measured and used in concert with a more sophisticated structure calculation program such as the HADDOCK docking simulation software (69), which can incorporate both PRE and RDC data. This has already been shown as a feasible approach in the structural modeling of the oxidized complex and can be extended to the reduced complex by modification of parameter and topology files for the metal cofactors in the reduced state of each protein. Efforts are currently ongoing in our group to collect these orientational restraints and utilize them in such a structure calculation protocol. Incorporation of RDCs is bound to increase the accuracy of the local structure and provide a means to elucidate the minute conformational differences that exist between the oxidized and reduced complexes in solution. More importantly, measurement of orientational constraints in multiple alignment media would enable us to measure even the dynamic changes that accompany these

conformational changes, since RDCs are sensitive to atomic motions on all timescales.

Uncovering the effector mechanism will likely require a better characterization of the dynamic differences between the two redox complexes. Such dynamic characterization is particularly important for perturbations upon complexation of highly dynamic regions such as the B'-Helix and the F-G Loop, that are observed in both our NMR study and the co-crystal structures (29). Conformational exchange in these secondary structures is expected to occur on the micro-millisecond timescales (70). Apart from the RDC measurements, chemical exchange experiments based on CPMG sequences can also provide helpful dynamic information on motions occurring in the micro- millisecond time regime (45). These experiments should also allow collecting dynamic information on regions inaccessible to our PRE experiments. If we can determine the exact nature of the conformation in each redox state for the complex in solution i.e. open or closed, then it may be possible to comprehensively describe the redox-modulated conformational changes propagated throughout CYP101 due to effector binding with the help of molecular dynamics (MD) simulations. These simulations have the potential of capturing differences in the conformational sampling of various states within the subtle secondary structure motions in the F-G Loop and B'-Helix that are responsible for substrate gating. Extracting redox-modulated exchange rates in these regions could provide compelling evidence in support of the conformational dynamics model of Pdx effector activity.

LIST OF REFERENCES

1. Sligar SG & Gunsalus IC (1976) Thermodynamic Model of Regulation - Modulation of Redox Equilibria in Camphor Monoxygenase. (Translated from English) *P Natl Acad Sci USA* 73(4):1078-1082 (in English).
2. Lyons TA, Ratnaswamy G, & Pochapsky TC (1996) Redox-dependent dynamics of putidaredoxin characterized by amide proton exchange. *Protein science : a publication of the Protein Society* 5(4):627-639.
3. Prudencio M & Ubbink M (2004) Transient complexes of redox proteins: structural and dynamic details from NMR studies. (Translated from English) *J Mol Recognit* 17(6):524-539 (in English).
4. Crowley PB & Ubbink M (2003) Close encounters of the transient kind: Protein interactions in the photosynthetic redox chain investigated by NMR spectroscopy. (Translated from English) *Accounts Chem Res* 36(10):723-730 (in English).
5. Reipa V, Mayhew MP, & Vilker VL (1997) A direct electrode-driven P450 cycle for biocatalysis. (Translated from eng) *Proc Natl Acad Sci U S A* 94(25):13554-13558 (in eng).
6. Omura T (2010) Structural diversity of cytochrome P450 enzyme system. (Translated from English) *J Biochem* 147(3):297-306 (in English).
7. Danielson PB (2002) The cytochrome P450 superfamily: Biochemistry, evolution and drug metabolism in humans. (Translated from English) *Curr Drug Metab* 3(6):561-597 (in English).
8. Guengerich FP & Munro AW (2013) Unusual cytochrome p450 enzymes and reactions. (Translated from eng) *J Biol Chem* 288(24):17065-17073 (in eng).
9. Munro AW, Girvan HM, Mason AE, Dunford AJ, & McLean KJ (2013) What makes a P450 tick? (Translated from English) *Trends in Biochemical Sciences* 38(3):140-150 (in English).
10. de Groot MJ (2006) Designing better drugs: predicting cytochrome P450 metabolism. (Translated from eng) *Drug Discov Today* 11(13-14):601-606 (in eng).
11. Scannell JW, Blanckley A, Boldon H, & Warrington B (2012) Diagnosing the decline in pharmaceutical R&D efficiency. (Translated from eng) *Nat Rev Drug Discov* 11(3):191-200 (in eng).
12. Raucy JL & Allen SW (2001) Recent advances in P450 research. (Translated from eng) *Pharmacogenomics J* 1(3):178-186 (in eng).
13. de Montellano PRO (2005) *Cytochrome P450: Structure, Mechanism, and Biochemistry* (Springer).
14. Gotoh O (1992) Substrate recognition sites in cytochrome P450 family 2 (CYP2) proteins inferred from comparative analyses of amino acid and coding nucleotide sequences. (Translated from eng) *J Biol Chem* 267(1):83-90 (in eng).
15. Sligar SG, Debrunner PG, Lipscomb JD, Namtvedt MJ, & Gunsalus IC (1974) A role of the putidaredoxin COOH-terminus in P-450cam (cytochrome m) hydroxylations. (Translated from eng) *Proc Natl Acad Sci U S A* 71(10):3906-3910 (in eng).

16. Poulos TL, Finzel BC, & Howard AJ (1987) High-resolution crystal structure of cytochrome P450cam. (Translated from eng) *J Mol Biol* 195(3):687-700 (in eng).
17. Zhang W, Pochapsky SS, Pochapsky TC, & Jain NU (2008) Solution NMR Structure of Putidaredoxin-Cytochrome P450cam Complex via a Combined Residual Dipolar Coupling-Spin Labeling Approach Suggests a Role for Trp106 of Putidaredoxin in Complex Formation. (Translated from English) *J Mol Biol* 384(2):349-363 (in English).
18. Sevrioukova IF, Poulos TL, & Churbanova IY (2010) Crystal structure of the putidaredoxin reductase x putidaredoxin electron transfer complex. (Translated from eng) *J Biol Chem* 285(18):13616-13620 (in eng).
19. Lipscomb JD, Sligar SG, Namtvedt MJ, & Gunsalus IC (1976) Autooxidation and hydroxylation reactions of oxygenated cytochrome P-450cam. (Translated from eng) *J Biol Chem* 251(4):1116-1124 (in eng).
20. Sevrioukova IF (2005) Redox-dependent structural reorganization in putidaredoxin, a vertebrate-type [2Fe-2S] ferredoxin from Pseudomonas putida. (Translated from English) *J Mol Biol* 347(3):607-621 (in English).
21. Pochapsky TC, Kostic M, Jain N, & Pejchal R (2001) Redox-dependent conformational selection in a Cys(4)Fe(2)S(2) ferredoxin. (Translated from English) *Biochemistry-Us* 40(19):5602-5614 (in English).
22. Pochapsky SS, Dang M, OuYang B, Simorellis AK, & Pochapsky TC (2009) Redox-Dependent Dynamics in Cytochrome P450(cam). (Translated from English) *Biochemistry-Us* 48(20):4254-4261 (in English).
23. Tyson CA, Lipscomb JD, & Gunsalus IC (1972) The role of putidaredoxin and P450 cam in methylene hydroxylation. (Translated from eng) *J Biol Chem* 247(18):5777-5784 (in eng).
24. Sligar SG, Lipscomb JD, Debrunner PG, & Gunsalus IC (1974) Superoxide anion production by the autoxidation of cytochrome P450cam. (Translated from eng) *Biochem Biophys Res Commun* 61(1):290-296 (in eng).
25. Rui LY, Pochapsky SS, & Pochapsky TC (2006) Comparison of the complexes formed by cytochrome P450(cam) with cytochrome b(5) and putidaredoxin, two effectors of camphor hydroxylase activity. (Translated from English) *Biochemistry-Us* 45(12):3887-3897 (in English).
26. Sevrioukova IF & Poulos TL (2011) Structural biology of redox partner interactions in P450cam monooxygenase: A fresh look at an old system. (Translated from English) *Arch Biochem Biophys* 507(1):66-74 (in English).
27. Tosha T, Yoshioka S, Ishimori K, & Morishima I (2004) L358P mutation on cytochrome P450cam simulates structural changes upon putidaredoxin binding: the structural changes trigger electron transfer to oxy-P450cam from electron donors. (Translated from eng) *J Biol Chem* 279(41):42836-42843 (in eng).
28. Nagano S, Tosha T, Ishimori K, Morishima I, & Poulos TL (2004) Crystal structure of the cytochrome p450cam mutant that exhibits the same

spectral perturbations induced by putidaredoxin binding. (Translated from eng) *J Biol Chem* 279(41):42844-42849 (in eng).
29. Pochapsky SS, Pochapsky TC, & Wei JW (2003) A model for effector activity in a highly specific biological electron transfer complex: The cytochrome P450(cam)-putidaredoxin couple. (Translated from English) *Biochemistry-Us* 42(19):5649-5656 (in English).
30. OuYang B, Pochapsky SS, Dang M, & Pochapsky TC (2008) A functional proline switch in cytochrome P450(cam). (Translated from English) *Structure* 16(6):916-923 (in English).
31. Wei JY, Pochapsky TC, & Pochapsky SS (2005) Detection of a high-barrier conformational change in the active site of cytochrome P450cam upon binding of putidaredoxin. (Translated from eng) *J Am Chem Soc* 127(19):6974-6976 (in eng).
32. Asciutto EK, Madura JD, Pochapsky SS, OuYang B, & Pochapsky TC (2009) Structural and Dynamic Implications of an Effector-induced Backbone Amide cis-trans Isomerization in Cytochrome P450(cam). (Translated from English) *J Mol Biol* 388(4):801-814 (in English).
33. Lyons TA, Ratnaswamy G, & Pochapsky TC (1996) Redox-dependent dynamics of putidaredoxin characterized by amide proton exchange. (Translated from English) *Protein Sci* 5(4):627-639 (in English).
34. Kuznetsov VY, Poulos TL, & Sevrioukova IF (2006) Putidaredoxin-to-cytochrome P450cam electron transfer: differences between the two reductive steps required for catalysis. (Translated from eng) *Biochemistry-Us* 45(39):11934-11944 (in eng).
35. Pochapsky SS, Pochapsky TC, & Wei JW (2003) A model for effector activity in a highly specific biological electron transfer complex: the cytochrome P450(cam)-putidaredoxin couple. *Biochemistry-Us* 42(19):5649-5656.
36. Sevrioukova IF, Li H, Zhang H, Peterson JA, & Poulos TL (1999) Structure of a cytochrome P450-redox partner electron-transfer complex. (Translated from eng) *Proc Natl Acad Sci U S A* 96(5):1863-1868 (in eng).
37. Tripathi S, Li H, & Poulos TL (2013) Structural basis for effector control and redox partner recognition in cytochrome P450. (Translated from eng) *Science* 340(6137):1227-1230 (in eng).
38. Muller JJ, Lapko A, Bourenkov G, Ruckpaul K, & Heinemann U (2001) Adrenodoxin reductase-adrenodoxin complex structure suggests electron transfer path in steroid biosynthesis. (Translated from eng) *J Biol Chem* 276(4):2786-2789 (in eng).
39. Guiles RD*, et al.* (1996) Pseudocontact shifts used in the restraint of the solution structures of electron transfer complexes. (Translated from English) *Nat Struct Biol* 3(4):333-339 (in English).
40. Crowley PB, Otting G, Schlarb-Ridley BG, Canters GW, & Ubbink M (2001) Hydrophobic interactions in a cyanobacterial plastocyanin-cytochrome f complex. (Translated from eng) *J Am Chem Soc* 123(43):10444-10453 (in eng).

41. Ubbink M, Ejdeback M, Karlsson BG, & Bendall DS (1998) The structure of the complex of plastocyanin and cytochrome f, determined by paramagnetic NMR and restrained rigid-body molecular dynamics. (Translated from eng) *Structure* 6(3):323-335 (in eng).
42. Gottstein D, Reckel S, Dotsch V, & Guntert P (2012) Requirements on paramagnetic relaxation enhancement data for membrane protein structure determination by NMR. (Translated from eng) *Structure* 20(6):1019-1027 (in eng).
43. Koehler J & Meiler J (2011) Expanding the utility of NMR restraints with paramagnetic compounds: background and practical aspects. (Translated from eng) *Prog Nucl Magn Reson Spectrosc* 59(4):360-389 (in eng).
44. Schlichting I*, et al.* (2000) The catalytic pathway of cytochrome p450cam at atomic resolution. (Translated from eng) *Science* 287(5458):1615-1622 (in eng).
45. Kleckner IR & Foster MP (2011) An introduction to NMR-based approaches for measuring protein dynamics. (Translated from English) *Bba-Proteins Proteom* 1814(8):942-968 (in English).
46. Fielding L (2003) NMR methods for the determination of protein-ligand dissociation constants. (Translated from eng) *Curr Top Med Chem* 3(1):39-53 (in eng).
47. Markwick PRL, Malliavin T, & Nilges M (2008) Structural Biology by NMR: Structure, Dynamics, and Interactions. (Translated from English) *Plos Comput Biol* 4(9) (in English).
48. Otting G (2010) Protein NMR Using Paramagnetic Ions. (Translated from English) *Annu Rev Biophys* 39:387-405 (in English).
49. Cheng H & Markley JL (1995) NMR spectroscopic studies of paramagnetic proteins: iron-sulfur proteins. (Translated from eng) *Annu Rev Biophys Biomol Struct* 24:209-237 (in eng).
50. Liang B, Bushweller JH, & Tamm LK (2006) Site-directed parallel spin-labeling and paramagnetic relaxation enhancement in structure determination of membrane proteins by solution NMR spectroscopy. (Translated from eng) *J Am Chem Soc* 128(13):4389-4397 (in eng).
51. Clore GM & Iwahara J (2009) Theory, practice, and applications of paramagnetic relaxation enhancement for the characterization of transient low-population states of biological macromolecules and their complexes. (Translated from eng) *Chem Rev* 109(9):4108-4139 (in eng).
52. Pintacuda G, Moshref A, Leonchiks A, Sharipo A, & Otting G (2004) Site-specific labelling with a metal chelator for protein-structure refinement. (Translated from English) *J Biomol Nmr* 29(3):351-361 (in English).
53. Gaponenko V, Altieri AS, Li J, & Byrd RA (2002) Breaking symmetry in the structure determination of (large) symmetric protein dimers. (Translated from English) *J Biomol Nmr* 24(2):143-148 (in English).
54. Holden M, Mayhew M, Bunk D, Roitberg A, & Vilker V (1997) Probing the interactions of putidaredoxin with redox partners in camphor p450 5-

monooxygenase by mutagenesis of surface residues. (Translated from English) *J Biol Chem* 272(35):21720-21725 (in English).
55. Lambeth DO & Palmer G (1973) The kinetics and mechanism of reduction of electron transfer proteins and other compounds of biological interest by dithionite. (Translated from eng) *J Biol Chem* 248(17):6095-6103 (in eng).
56. Greenbau.E, Gunsalus IC, Austin RH, & Frauenfe.H (1972) Photoreduction of Nadp+ Sensitized by Synthetic Pigment Systems. (Translated from English) *P Natl Acad Sci USA* 69(5):1273-& (in English).
57. Bertini I, Luchinat C, Parigi G, & Pierattelli R (2008) Perspectives in paramagnetic NMR of metalloproteins. (Translated from eng) *Dalton Trans* (29):3782-3790 (in eng).
58. Battiste JL & Wagner G (2000) Utilization of site-directed spin labeling and high-resolution heteronuclear nuclear magnetic resonance for global fold determination of large proteins with limited nuclear overhauser effect data. (Translated from eng) *Biochemistry-Us* 39(18):5355-5365 (in eng).
59. Zhang W, Pochapsky SS, Pochapsky TC, & Jain NU (2008) Solution NMR structure of putidaredoxin-cytochrome P450cam complex via a combined residual dipolar coupling-spin labeling approach suggests a role for Trp106 of putidaredoxin in complex formation. *Journal of molecular biology* 384(2):349-363.
60. Aoki M, Ishimori K, & Morishima I (1998) NMR studies of putidaredoxin: associations of putidaredoxin with NADH-putidaredoxin reductase and cytochrome p450cam. (Translated from eng) *Biochim Biophys Acta* 1386(1):168-178 (in eng).
61. Dvoretsky A, Gaponenko V, & Rosevear PR (2002) Derivation of structural restraints using a thiol-reactive chelator. (Translated from eng) *Febs Lett* 528(1-3):189-192 (in eng).
62. Gaponenko V*, et al.* (2004) Improving the accuracy of NMR structures of large proteins using pseudocontact shifts as long-range restraints. (Translated from eng) *J Biomol Nmr* 28(3):205-212 (in eng).
63. Ikegami T*, et al.* (2004) Novel techniques for weak alignment of proteins in solution using chemical tags coordinating lanthanide ions. (Translated from eng) *J Biomol Nmr* 29(3):339-349 (in eng).
64. Page CC, Moser CC, Chen X, & Dutton PL (1999) Natural engineering principles of electron tunnelling in biological oxidation-reduction. (Translated from eng) *Nature* 402(6757):47-52 (in eng).
65. Volkov AN, Worrall JAR, Holtzmann E, & Ubbink M (2006) Solution structure and dynamics of the complex between cytochrome c and cytochrome c peroxidase determined by paramagnetic NMR. (Translated from English) *P Natl Acad Sci USA* 103(50):18945-18950 (in English).
66. Aoki M, Ishimori K, & Morishima I (1998) Roles of negatively charged surface residues of putidaredoxin in interactions with redox partners in p450cam monooxygenase system. (Translated from eng) *Biochim Biophys Acta* 1386(1):157-167 (in eng).

67. Unno M, Shimada H, Toba Y, Makino R, & Ishimura Y (1996) Role of Arg112 of cytochrome p450cam in the electron transfer from reduced putidaredoxin. Analyses with site-directed mutants. (Translated from eng) *J Biol Chem* 271(30):17869-17874 (in eng).
68. Lee YT, Wilson RF, Rupniewski I, & Goodin DB (2010) P450cam visits an open conformation in the absence of substrate. (Translated from eng) *Biochemistry-Us* 49(16):3412-3419 (in eng).
69. de Vries SJ, van Dijk M, & Bonvin AM (2010) The HADDOCK web server for data-driven biomolecular docking. (Translated from eng) *Nat Protoc* 5(5):883-897 (in eng).
70. Mittermaier AK & Kay LE (2009) Observing biological dynamics at atomic resolution using NMR. (Translated from eng) *Trends Biochem Sci* 34(12):601-611 (in eng).

APPENDIX

Table 1. PRE Measurements for Pdx^{r} and back calculated distances from Pdx^{r} crystal structure (PDB I.D. 1XLQ)

Residue no.	Measured (Å)	Calculated (Å)
3	32.8	34.8
4	32.9	33.7
6	30.3	31.4
7	29.7	31.8
8	30.3	31.9
9	31.5	30.4
18	32.5	31
21	32.3	30.7
22	28.4	27.9
31	32.5	33.4
33	29.4	30.1
35	28.2	28.3
51	27.5	26.1
52	25.2	23.7
53	24.9	24.8
54	29.4	28.1
56	31	29.4
58	30.7	30.6
58	29.7	28.2
59	29.8	29.4
60	30.6	29.1
62	28.3	27.5
63	24.6	22.7
78	23.5	19.1
79	22.6	21
81	24.1	22.4
83	24.4	20.5
90	31.2	29.3
89	28.2	27.3
103	25.5	25.6
105	23.7	21.8
106	22.6	20.4

[a]Distances are measured from the intensity ratios calculated for the HN backbone amide resonances of ^{15}N labeled Pdx^{r} conjugated with EDTA spin label and coordinated to Gd^{3+}. Error bounds of ± 4Å were applied to every measurement.

VITA

Nicholas John Lopes was the second of three sons born to Anthony and Cathy Lopes on August 9, 1985 in Miami, FL. At six months of age he moved with his family to Germantown, TN, a quaint suburb of Memphis, TN. There he attended public school at Dogwood Elementary and Houston Middle, before receiving a college-preparatory education at Christian Brothers High School, an all-boy, catholic school of the Lasallian tradition. Immediately following high school graduation in 2004, he enrolled at the University of Tennessee, Knoxville (UTK). After vacillating between majors for a year he settled on Ecology and Evolutionary Biology. It was his decision to volunteer at a microbiology laboratory in the Center for Environmental Biotechnology (CEB) at UTK during his junior year that set him on the path of academic research. While continuing his work at the CEB, Nicholas received his Bachelor's degree in 2008. After spending one additional year as a research technician with the CEB, he accepted an offer to enter the Biochemistry, Molecular and Cellular Biology Department graduate program at UTK. Upon receiving his Master's degree he hopes to continue pursuing his dream of leading an interesting life.